Aeroacoustic Computations of a Generic Low Boom Concept in Landing Configuration: Part 3 - Aerodynamic Validation and Noise Source Identification

Mehdi R. Khorrami[1], Patrick R. Shea[2], Courtney S. Winski[2]
NASA Langley Research Center, Hampton, VA, 23681, USA

Patricio A. Ravetta[3]
AVEC Inc., Blacksburg, VA 24060, USA

André F. P. Ribeiro[4]
Dassault Systèmes *GmbH, 70563, Stuttgart, Germany*

Ryan Ferris[5]
Dassault Systèmes*, Long Beach, CA, 90802, USA*

Michael Sacks[6]
Dassault Systèmes, Waltham, MA 02451, USA

Wind tunnel test data were used to validate the predicted aerodynamic behavior of a 15%-scale version of a generic, low-boom aircraft. The test was conducted in the NASA Langley 14- by 22-Foot Subsonic Tunnel to determine the low-speed aerodynamic characteristics of the model. Measured steady surface pressures and global forces were used to validate predicted aerodynamic results obtained from high-fidelity simulations of the model as installed in the tunnel. Very good agreement between predicted and measured aerodynamic trends was demonstrated, providing the impetus to proceed with companion airframe noise simulations that were conducted in a free-air setting. Computed near-field flow variables acquired on a permeable data surface were used to generate synthetic pressure records for two 800-element phased microphone arrays positioned overhead and to the side of the model. The array data were beamformed to generate noise source localization maps for the clean model and several landing configurations. Primary and secondary airframe sources were identified and their relative strengths were determined. Far-field integrated noise spectra for the full aircraft, as well as individual components, were obtained from the source maps via integration of tailored regions. The analysis showed that noise produced by the landing gear was the dominant contributor to the far-field acoustic signature of the model, followed by flap noise. The effects of permeable data surface end caps, spatial resolution, array orientation, angle of attack, component interaction, velocity scaling, and numerical precision on synthetic far-field spectra were also evaluated.

[1] Senior Scientist, Computational AeroSciences Branch, Associate Fellow AIAA.
[2] Aerospace Engineer, Configuration Aerodynamics Branch, Senior Member AIAA.
[3] Co-owner, Chief Research Engineer, Senior Member AIAA.
[4] Industry Process Senior Specialist, SIMULIA Aerospace & Defense.
[5] SIMULIA Industry Process Consultant, SIMULIA NAM 3DX Fluids, AIAA Member.
[6] Fluids Industry Process Expert Specialist, AIAA Member.

I. Nomenclature

14x22	=	NASA Langley 14- by 22-Foot Subsonic Tunnel
AL	=	Left Aileron
AoA	=	Angle of Attack
AR	=	Right Aileron
C_L	=	Lift Coefficient without tunnel wall corrections
C_D	=	Drag Coefficient without tunnel wall corrections
C_m	=	Pitching Moment Coefficient without tunnel wall corrections
FA	=	Free Air
FL	=	Left Flap
FR	=	Right Flap
FW-H	=	Ffowcs-Williams and Hawkings
GLBC	=	Generic Low Boom Concept
HL	=	Left Stabilator
HR	=	Right Stabilator
IGE	=	In Ground Effect
LaRC	=	Langley Research Center
LGoff	=	Landing Gear Stowed
LGon	=	Landing Gear Deployed
M	=	Mach Number
OGE	=	Out of Ground Effect
Re	=	Reynolds Number

II. Introduction

Several efforts are under way within the aviation industry to develop early entrants into the commercial supersonic business jet market [1, 2]. The introduction of new aircraft types requires compliance with stringent national and international regulations that limit excessive aircraft noise. This increased activity has prompted regulatory bodies, such as the International Civil Aviation Organization and the US Federal Aviation Administration, to commence the laborious task of developing the necessary standards and metrics that would regulate the impact of supersonic aircraft operations during landing and takeoff on communities near airports. The lack of experimental and computational data on noise generated by supersonic aircraft may induce the regulatory bodies to rely on system-level acoustic analyses generated from existing semiempirical prediction models that were developed for conventional tube-and-wing subsonic aircraft [3]. As such, these analyses contain a significant level of uncertainty. The availability of semiempirical noise prediction models that have been fine-tuned for supersonic aircraft is crucial to the execution of parametric studies that evaluate competing concepts and identify the most viable low-noise configurations. The present multiphase investigation represents a first step in a focused effort by NASA to create a much-needed database on the airframe component of noise generated by commercial supersonic transports and, thus, improve the state-of-the-art in noise prediction tool development.

Currently, there are significant gaps in our understanding of the airframe noise signature of commercial supersonic transports during landing. Due to the dearth of experimental studies, very little is known on the nature of primary and secondary airframe noise sources and their contribution to far-field acoustic behavior. Among the earliest airframe noise investigations of commercial supersonic aircraft was the test performed by Preisser [4] in an anechoic flow facility at the NASA Langley Research Center (LaRC). A 1.5%-scale model of an advanced supersonic transport concept (AST-100) in landing configuration was tested to determine far-field noise levels and the effects of gear and flap deployment on the noise signature. Two decades later, Herkes and Stoker [5] used a 3%-scale model of the High-Speed Civil Transport to acquire far-field acoustic data. Major airframe noise sources were identified from phased microphone array measurements. Although early investigations like these provided valuable information into the acoustic behavior of supersonic transports at low speeds, the extremely small scale of the models and the high-passenger count of the concepts severely limit their application to the study of supersonic business jets. For example, the far-field spectra measured in Ref. [4] are below 250 Hz at full-scale frequencies.

Also absent from the available literature are detailed computational airframe noise studies of supersonic business jets in landing configuration. Numerical simulations of high physical fidelity have made significant inroads as a viable, complementary tool to wind tunnel testing for airframe noise characterization. Previous efforts conducted under the NASA Environmentally Responsible Aviation and Flight Demonstrations and Capabilities projects clearly established the applicability of physics-based computational simulations to two essential aspects of airframe noise prediction for sub- and full-scale subsonic aircraft in landing configuration: identification of primary and secondary sources and generation of accurate far-field noise footprints [6-9]. The vetted accuracy and wide acceptance of high-fidelity simulations provide ample justification for exploratory airframe noise predictions to lower the uncertainty in system-level acoustic analyses of supersonic transports until complementary experimental tests can be performed. Thus, the present investigation aims to extend the computational methodology used in our previous studies to commercial supersonic aircraft concepts to better understand the relevance of airframe sources to the far-field noise footprint of this transport class. After extensive consideration, a generic low boom concept (GLBC) was selected as the testbed for this initial study. Although not a viable passenger-carrying supersonic business jet, two important attributes heavily tilted the selection process in favor of the GLBC. First, the chosen concept is an earlier version of the low-boom X-59 supersonic demonstrator being built for NASA [10]. Thus, if the opportunity arises, aeroacoustic data could be acquired at full-scale to validate the efficacy of the computational approach. Second, a 15%-scale model of the GLBC was tested in the NASA LaRC 14- by 22-Foot Subsonic Tunnel (14x22) to determine the low-speed aerodynamic characteristics of the configuration prior to building the X-59 plane. Although not from an acoustic test, the measured data provide sufficient information to validate predicted aerodynamic trends before embarking on the more challenging and costly airframe noise simulations.

The present study was executed in three phases. Given the vast differences between the flow fields of low aspect ratio supersonic wings and those of conventional subsonic aircraft, the initial phase focused on accurately predicting the key aerodynamic characteristics of the GLBC. To facilitate comparisons with measured data, this phase required that the wind tunnel test section and model support system be included in the simulations [11]. The second phase of our effort targeted the prediction of airframe noise by conducting free-air simulations of the GLBC in various landing configurations [12] to determine the contribution of various airframe components, individually and combined, to the far-field noise footprint of the model.

The present paper summarizes the work conducted during the third phase of the effort and includes descriptions of the following aspects: a GLBC test in the 14x22 tunnel, tabulation of the experimental data, validation of the predicted aerodynamic trends, and identification and ranking of the computed airframe noise sources via a specially designed synthetic phased microphone array.

III. Description of Wind Tunnel Stability and Control Test

In this section, we provide a condensed description of the aircraft model, test setup in the LaRC 14x22 tunnel, acquired data, and configurations selected for validation of the simulated aerodynamic results.

A. Test Overview

A low-speed stability and control test of an early prototype of the Quiet Supersonic Technology X-59 Low-Boom Flight Demonstrator aircraft was performed at the LaRC 14x22 in the fall of 2017. The focus of the test was to assess the low-speed flight characteristics of the model over a range of pitch and sideslip angles, evaluate the control surface effectiveness on the vehicle aerodynamics at low speeds, and assess the vehicle stability and control in ground effect conditions with multiple landing gear and landing gear door configurations. These data were used both to guide design revisions to help improve the low-speed flight characteristics of the vehicle during takeoff and landing, and to help develop the X-59 flight control system. For clarity and consistency with Refs. [11, 12], the tested model will be referred to as GLBC for the remainder of this paper.

B. Model Description

The wind tunnel test article was a 15%-scale model of the GLBC C608 outer mold line. The reference parameters for the model-scale vehicle are provided in Table 1, and a three-view with model scale dimensions of the test article is presented in Fig.1. The wind tunnel model was fabricated by Tri Models, Inc. and designed with a focus on force and moment testing in and out of ground effect (IGE, OGE). The model was sting mounted with an internal balance. A photograph of the OGE test installation is shown in Fig. 2, and a photograph of the IGE test configuration with landing gear installed and flaps deflected is presented in Fig. 3.

Table 1. Reference parameters for 15%-scale GLBC wind tunnel model.

Parameter	Value
Reference Area [in^2]	1575.158
Reference Span [in]	53.100
Reference Chord [in]	39.528

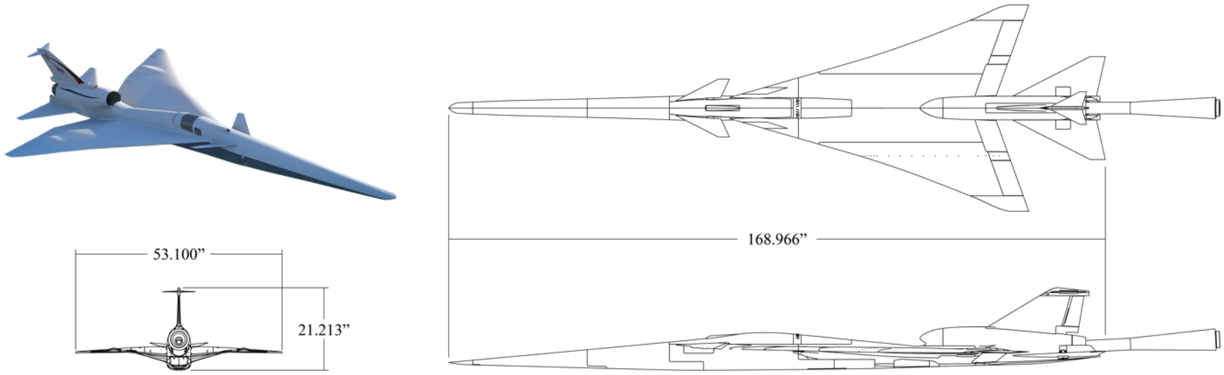

Fig. 1 Three-view drawing of 15%-scale low-speed wind tunnel model and artist rendering of the GLBC flight vehicle.

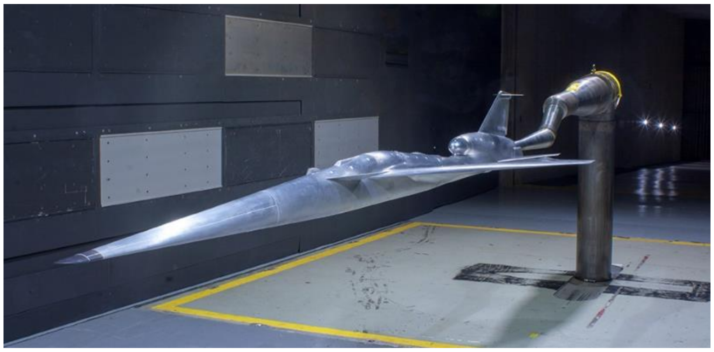

Fig. 2 GLBC model configured for OGE testing in the LaRC 14x22 tunnel.

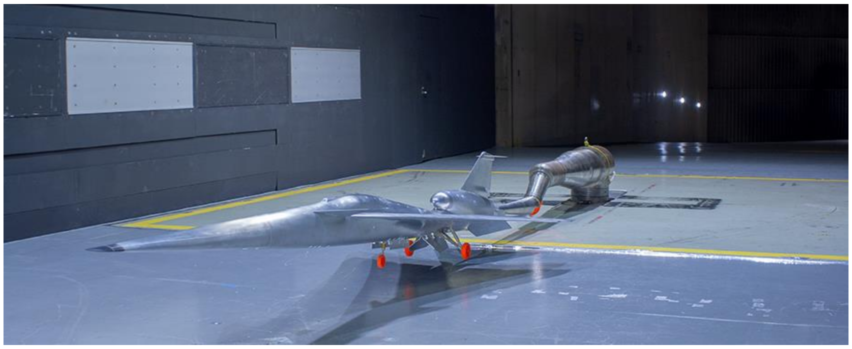

Fig. 3 GLBC model configured for IGE testing in the LaRC 14x22 tunnel.

The model was designed to test the stability and control of the aircraft with different control surface settings (see Figs. 4 and 5 for control surface locations and naming convention). The flaps, ailerons, t-tail, and rudder were designed such that each control surface deflection setting was a unique model part that could be installed as desired (for example, to change from the 0° flap setting to the 30° flap setting required the removal of the 0° flap and the installation of the 30° flap). The stabilators could also be set to different control surface deflections, but these were set using a geared attachment point with indexed locations. For all control surface deflections, a positive deflection was defined with the trailing edge down, or in the case of the rudder, trailing edge to the port side.

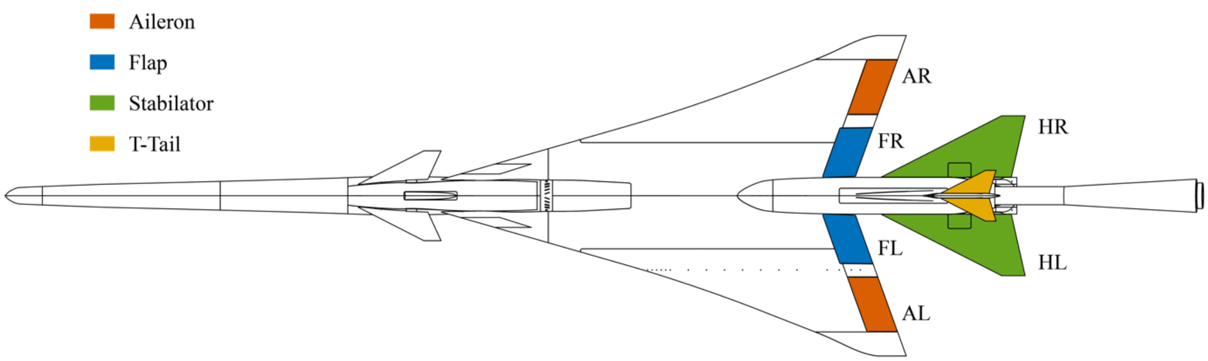

Fig. 4 Top view of GLBC model with control surfaces highlighted.

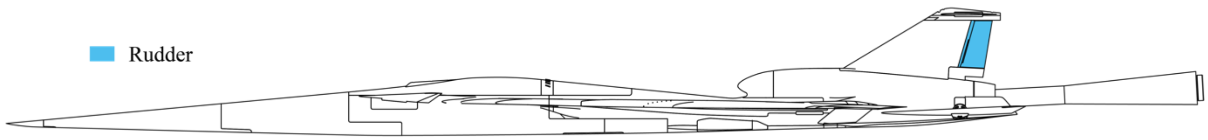

Fig. 5 Side view of GLBC model with control surfaces highlighted.

C. Instrumentation

The main instrumentation for the test was a 6-component force and moment balance installed in the model. The balance used for the test was the NASA LaRC 1621B balance, which is a single-piece moment balance with capacities listed in Table 2. The balance was recalibrated in 2017 prior to the 14x22 test entry.

Table 2. Balance capacities for the Langley 1621B balance.

Normal Force [lb]	Side Force [lb]	Axial Force [lb]	Rolling Moment [in-lb]	Pitching Moment [in-lb]	Yawing Moment [in-lb]
3000	1800	500	7500	10000	4500

The model was instrumented with 24 pressure taps in a single streamwise row on the port wing between the flap and aileron (see Fig. 4), 4 pressure taps on the base of the model where the sting entered, and 4 internal cavity pressures. These 32 pressure taps were connected to an electronically scanned pressure (ESP) module mounted in the model for the duration of testing. The 4 base and 4 cavity pressures were used to correct the axial force and pitching moment data. The 24 surface pressures on the wing were acquired for CFD validation.

The model angles were computed from the support system hardware angles, which were measured using the pitch strut, yaw table, and roll mechanism angle resolvers with sting bending and balance deflection corrections evaluated using the model loads measured by the balance. The uncertainties of the pitch and roll angle calculations, including sting and balance deflections, were measured to be less than ±0.01° during pretest assessments. The model had two onboard Q-flex sensors that were also used to measure the model pitch and roll angles. These onboard measurements were used as validation of the angles computed from the support system that were used as the primary measurements of pitch, yaw, and roll.

D. Boundary Layer Tripping

The boundary layers on the fuselage, canards, wings, stabilators, vertical stabilizer, t-tail and engine fairing were tripped to force turbulent boundary layer development. The transition dots on the fuselage were arranged as rings at two axial stations on the nose with two linear strips connecting the two rings. This pattern was selected to force transition for all of the pitch and yaw angles tested. For the canards, wings, stabilators, vertical stabilizer and t-tails, a row of trip dots was placed on both the pressure and suction surfaces at a fixed distance from the leading edge of each airfoil section. Transition dots were arranged in a single row around the circumference of the nacelle fairing. The transition dots used on the fuselage nose, wings, and nacelle fairing had a height of 0.0081 inches. The transition dots used on the canards, stabilators, vertical stabilizer, and t-tails had a height of 0.0060 inches.

E. Data Reduction

The data reduction methodology for the test was developed to compute the most accurate representation of the free-air force and moment coefficients possible. Best practices for balance data acquisition were implemented including weight tare measurements and corrections, regular acquisition of wind-off-zeros throughout the test, and balance temperature compensation. A number of standard corrections were applied to the balance data including flow angularity, buoyancy, and base and cavity pressures. Model attitude (pitch and yaw) was corrected for flow angularity. Freestream facility conditions including Mach number, dynamic pressure, static pressure, and static temperature were measured or computed using the best practices of the facility.

F. Selected Configurations for Airframe Noise Prediction

To map out the stability and control of the aircraft, numerous model configurations in the OGE and IGE settings were tested resulting in an extensive database. For the purposes of airframe noise prediction, only a small subset of configurations in the OGE setting were considered. Four configurations were selected: flap 0° with landing gear stowed (LGoff), flap 30° with landing gear deployed (LGon), flap 0° with LGon, and flap 30° with LGoff. Configuration Flap0-LGoff corresponds to an aircraft in cruise and represents the quietest possible (baseline) configuration, while Flap30-LGon corresponds to a landing scenario as shown in Fig. 6. The other two configurations, Flap30-LGoff and Flap0-LGon, serve to isolate the effects of flaps and landing gear on far-field noise. The four selected geometries are listed in Table 3 along with their corresponding test run numbers. The experimental data used to validate the simulated aerodynamic results were extracted from these runs.

Table 3. Configurations studied.

	Flap Angle	Landing Gear	Test Run No.
Flap0-LGoff	0°	Stowed	159
Flap30-LGoff	30°	Stowed	271
Flap0-LGon	0°	Deployed	424
Flap30-LGon	30°	Deployed	431

Fig. 6 GLBC model with flaps deflected 30° and landing gear deployed (landing condition) configured for OGE testing in the LaRC 14x22 tunnel.

IV. Experimental and Computational Data Sets

A description of the experimental and computational data sets used to validate the predicted aerodynamic trends is provided in this section. Relevant issues such as tunnel wall effects, quality, repeatability, and uncertainty of the measured values, as well as numerical uncertainties due to spatial resolution effects are addressed and discussed.

A. Experimental Data

The experimental data set comprises aerodynamic measurements only, since the purpose of the 2017 GLBC test in the 14x22 tunnel was to assess the stability and control characteristics of the model. Acoustic measurements were not obtained. The aerodynamic data consist of steady surface pressure measurements acquired on a set of pressure ports at a single streamwise row on the wing port side (Fig. 4) and overall forces and moments. Of this data set, only measurements from the tunnel runs corresponding to the four configurations in OGE listed in Table 3 were used to validate predicted results. The corrections imposed to account for tunnel wall effects were deemed negligible. Therefore, uncorrected lift, drag, and pitching moment coefficients (no base pressure, cavity pressure, or tunnel wall effect corrections – C_L, C_D, and C_m) were used in direct comparisons with simulated data. All experimental data used in this investigation correspond to a nominal Mach number M = 0.2.

1. Data Quality and Repeatability

The quality and repeatability of the measured aerodynamic data are of paramount importance to a successful validation of the simulated results. Unfortunately, three of the selected configurations were evaluated with only a single test run (Flap30-LGoff), one (Flap30-LGon) repeat run, and two (Flap0-LGon) repeat runs. In contrast, parsing through the vast amount of data acquired for Flap0-LGoff (cruise) during the 2017 tunnel entry, in addition to R159, five other runs were identified that could serve as repeat data for this configuration. The repeatability of measured integrated forces and pitching moment for the Flap0-LGoff configuration is demonstrated in Fig. 7. Overall, very good data collapse for C_L, C_D, and C_m is observed over the entire angle of attack (AoA) range tested. The largest deviation, which occurs in the C_L values at higher AoAs, is associated solely with R438 data. This deviation is slightly more visible in the drag polar of Fig. 7d. Nevertheless, considering the number of configuration changes that occurred during the 2017 tunnel entry, the quality and repeatability of the measured forces for the cruise configuration are exceptionally good.

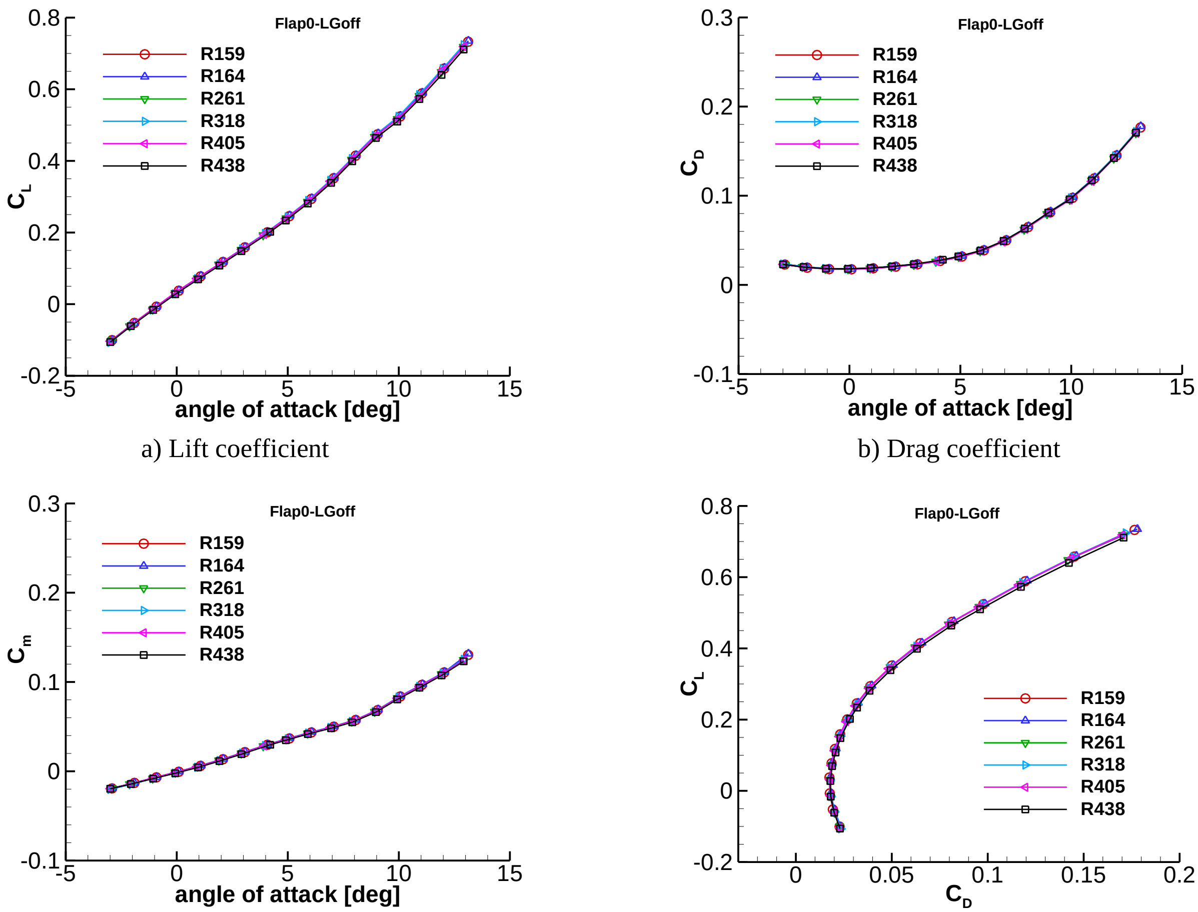

a) Lift coefficient

b) Drag coefficient

c) Pitching moment coefficient

d) Drag polar

Fig. 7 Repeat measurements of lift, drag, and pitching moment of GLBC model for Flap0-LGoff configuration.

The landing condition, which represents the noisiest airframe configuration, is of paramount importance to the present study. The aerodynamic coefficients for the Flap30-LGon (landing) and Flap0-LGon model configurations are shown in Figs. 8 and 9, respectively. Based on a very limited number of runs, similar data repeatability as that obtained for the Flap0-LGoff (cruise) configuration is observed. Although not shown, the pitching moment coefficient and drag polar plots for Flap0-LGon (Fig. 9) indicated similar data collapse as those for the lift and drag coefficients.

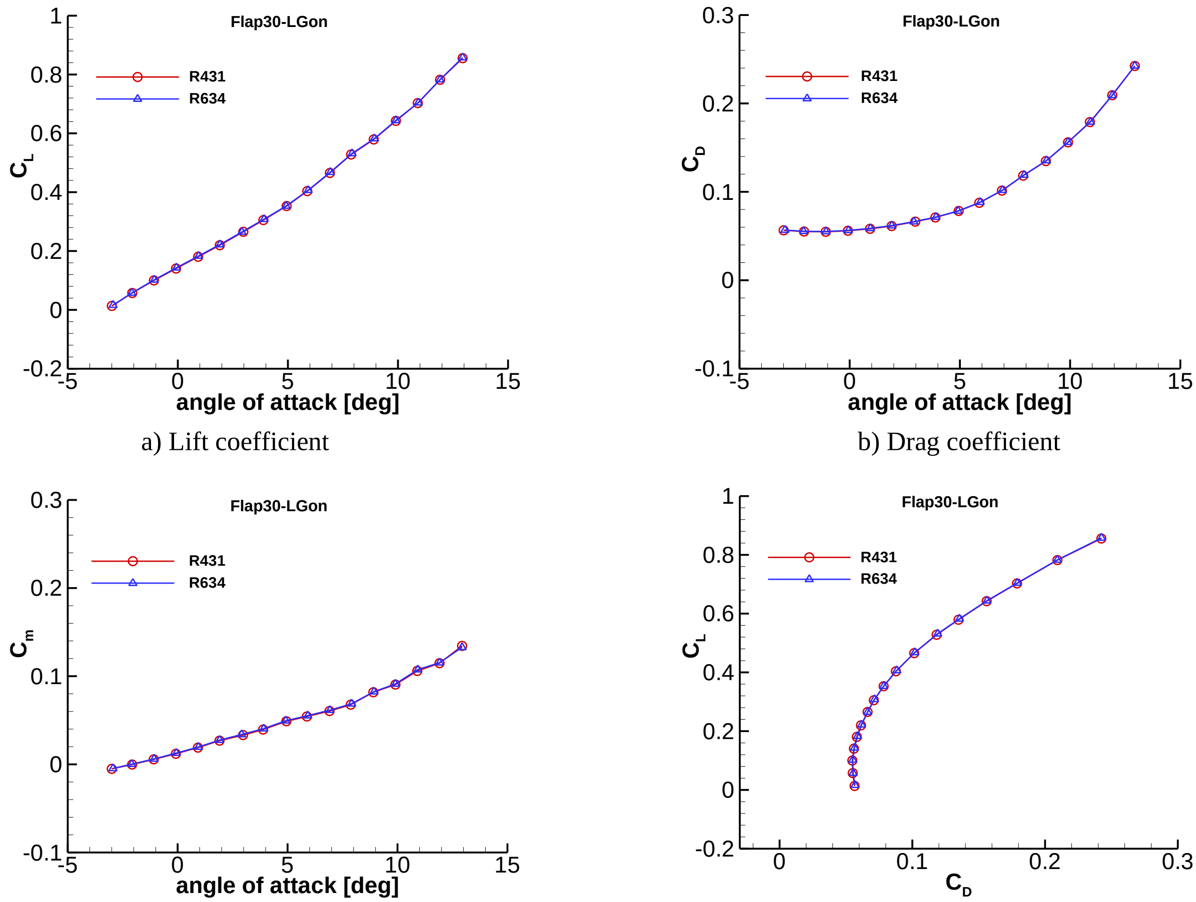

a) Lift coefficient b) Drag coefficient

c) Pitching moment coefficient d) Drag polar

Fig. 8 Repeat measurements of lift and drag of GLBC model for Flap30-LGon configuration.

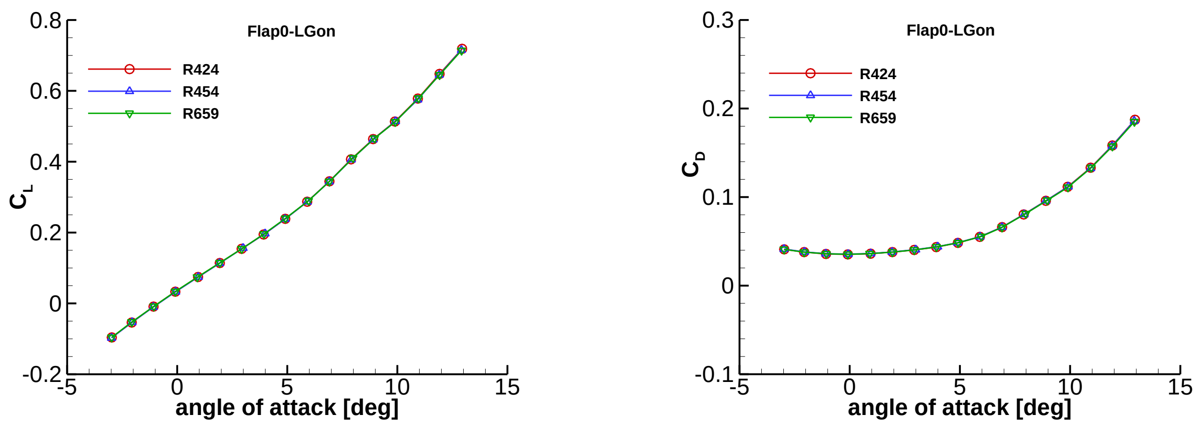

a) Lift coefficient b) Drag coefficient

Fig. 9 Repeat measurements of lift and drag of GLBC model for Flap0-LGon configuration.

Because of suboptimal aerodynamic performance at low speeds, supersonic aircraft generally land at higher AoA than a typical subsonic transport. Initially, our goal was to conduct the simulations at an AoA of 11°. However, examination of measured surface pressures for the Flap0-LGoff configuration revealed that the pressure distribution at these higher angles is sensitive to small variations in AoA. This sensitivity is clearly shown in Fig. 10a, where the pressure coefficient (C_p) distribution on the wing from all the repeat runs at a “nominal” AoA = 11° are compared. Setting the model to the exact “nominal” setpoint is not critical for force and moment testing, which was the primary test objective, so long as the actual setpoint calculation is precise. For testing efficiency, the model was set close to the "nominal" AoA but was not required to be exact, which resulted in minute variations in AoA for each test run from the "nominal," as seen in Fig. 10a. Despite actual setpoint variations less than ±0.1° in AoA, observe the significant variations in the suction peak on the wing suction surface that were induced by the primary vortex near the leading edge. The vortex suction seen in Fig. 10a is noticeably higher for those runs having an AoA slightly lower than 11°. Note that the lines connecting the data points are for clarity only, and do not imply that C_p can be linearly interpolated between the experimental points.

The sensitivity to small AoA variations and the resulting effect in C_p distribution for the cruise configuration, even in the presence of tripped model leading edges (e.g., wing, canard, tail); and the lack or limited number of repeat runs for the other configurations, raised concerns regarding suitability of data collected at AoA = 11° for validation of computational results. To substantially reduce the chances of dealing with C_p distributions that are too close to a bifurcation point, we decided to conduct the airframe noise simulations at AoA = 9°. Since the airframe noise signature of an aircraft is very weakly dependent on AoA at low and moderate angles [13], simulations performed at AoA = 9° would provide the desired insights and knowledge into the acoustic characteristics of supersonic aircraft during landing. To illustrate the advantages of lowering AoA by 2°, measured C_p distributions for the Flap0-LGoff configuration at the "nominal" angle of 9° are shown in Fig. 10b. As can be seen, despite similar variations in the model AoA, the C_p values obtained from the six test runs collapse very well, thus depicting a good, repeatable set of data. Corresponding surface pressure distributions for Flap30-LGon and Flap0-LGon at the "nominal" angle of 9° are displayed in Fig. 11. Based on the limited number of runs available, a good, repeatable set of measured pressures is depicted in these plots.

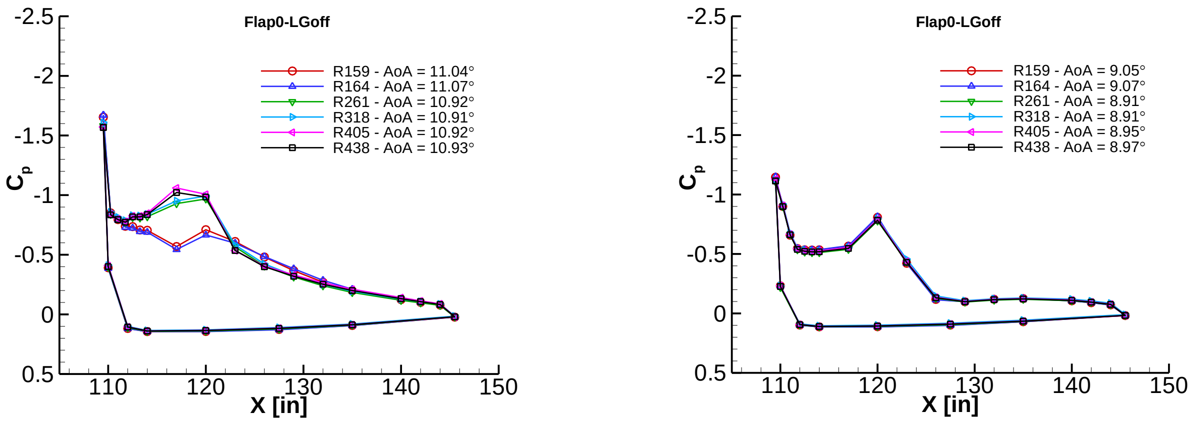

a) AoA = 11° b) AoA = 9°

Fig. 10 Streamwise pressure distributions from repeat runs of GLBC for Flap0-LGoff configuration.

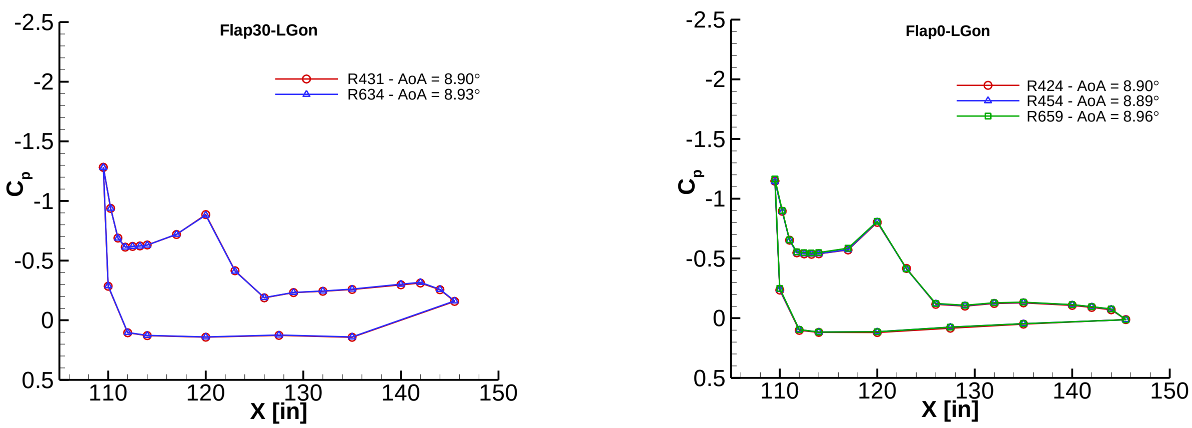

a) Flap30-LGon b) Flap0-LGon

Fig. 11 Streamwise pressure distributions from repeat runs of GLBC for Flap30-LGon and Flap0-LGon configurations at AoA = 9°.

Direct comparisons of measured force and pitching moment coefficients for the four selected GLBC configurations are presented in Fig. 12. As is the case for subsonic aircraft, the lift produced by the model increased by a constant amount with flap deflection (Fig. 12a). Note also that landing gear deployment caused a slight degradation in lift coefficient, especially at higher AoA, when flaps are deflected also, pointing to potential gear-flap flow interaction. Observe from Fig. 12b that simultaneous deployment of flaps and landing gear increased model drag; however, while the drag rise caused by gear deployment remains fairly constant over the AoA range tested, at higher AoAs, the drag rise from flap deflection becomes significantly larger than the corresponding increase due to gear deployment.

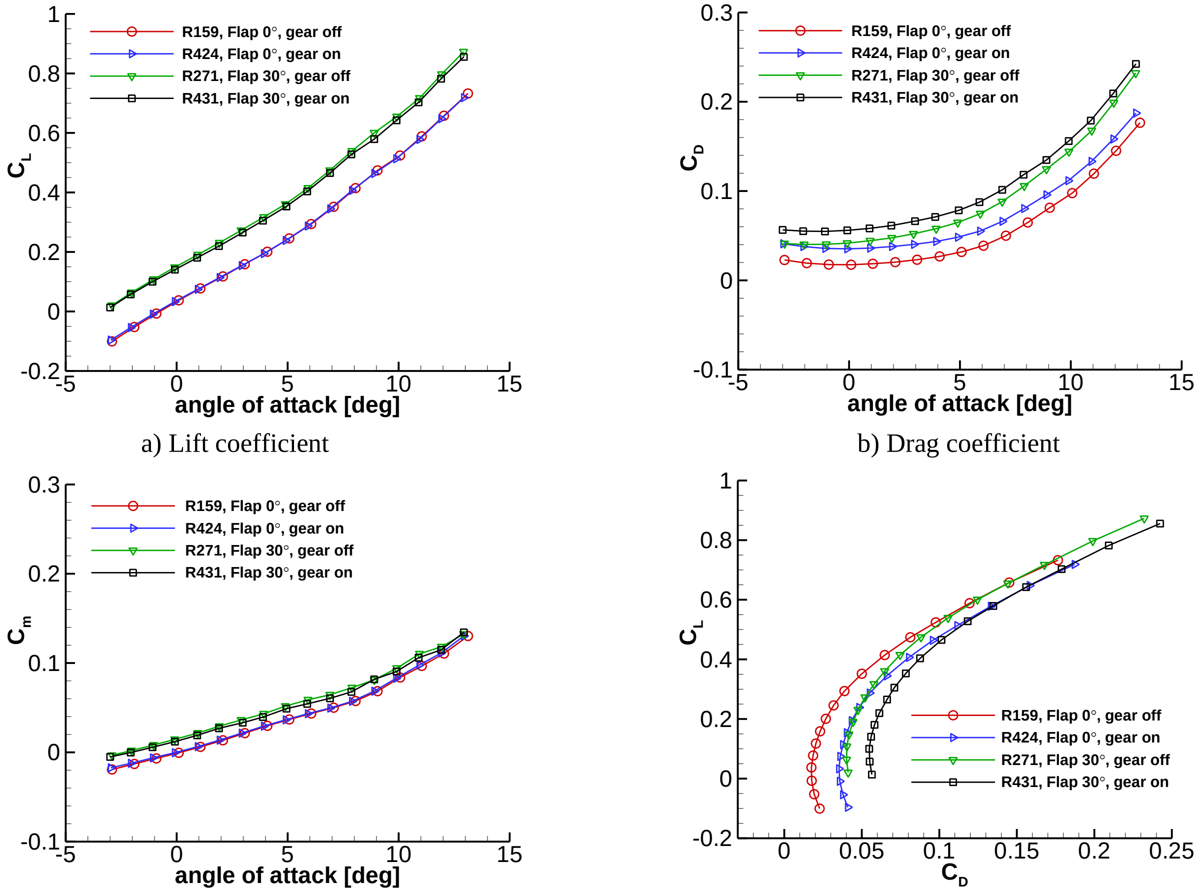

a) Lift coefficient

b) Drag coefficient

c) Pitching moment coefficient

d) Drag polar

Fig. 12 Lift, drag, and pitching moment of GLBC model for selected configurations.

B. Computational Data

All synthetic data presented in section V were extracted from the PowerFLOW® simulations described in Refs. [11] and [12]. In section V.A, predicted results obtained from the simulations of Ref. [11] were used for aerodynamic validation. For these computations, the 14x22 tunnel contraction section, test section, and the initial portion of the first diffuser were accurately modeled from available laser scans of the facility walls and included in the simulations. Also, integral to the simulated geometry was a high-fidelity, digital representation of the model support system developed from engineering drawings. A schematic representation of the computational domain and a close-up image of the CAD model in landing configuration as installed in the 14x22 tunnel are presented in Fig. 13. The aerodynamic simulations were mostly focused on Flap0-LGoff and Flap30-LGon, the two configurations of interest representing the quietest (cruise) and noisiest (landing) conditions, respectively. The simulated ambient parameters were set to values corresponding to the selected GLBC test runs. Most computations were executed at two grid resolution levels ("coarse" and "medium", corresponding to 1.5 billion and 5 billion cells, respectively) to determine the effect of spatial resolution on predicted aerodynamic trends. For our most critical case of Flap30-LGon at AoA = 9°, an additional simulation was performed at a higher resolution level ("fine", 17 billion cells).

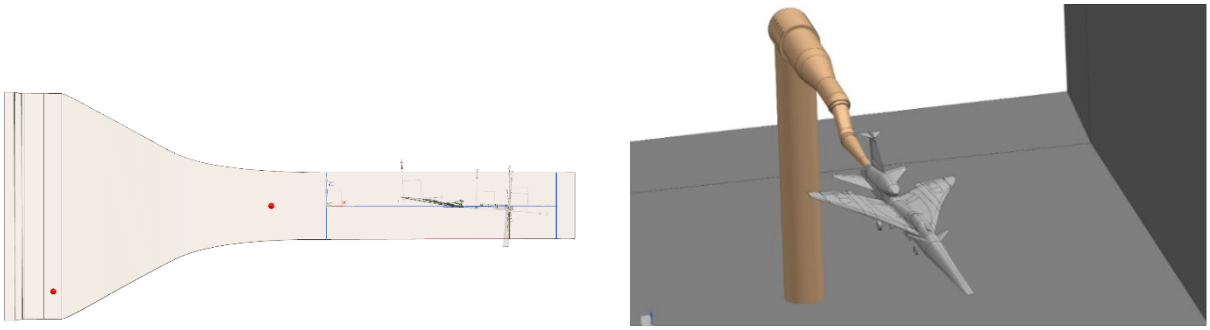

a) Simulated wind tunnel sections b) Installed GLBC

Fig. 13 Close-up image of GLBC CAD model with flaps deflected at 30° and landing gear deployed (landing condition) as installed in the LaRC 14x22 tunnel.

Data used for the aeroacoustic analyses of section V.B were leveraged from the airframe noise simulations described in Ref. [12]. These simulations were performed in free-air conditions, without the wind tunnel and model support system (see Fig. 14), to eliminate reflections from walls and allow the acoustic waves to propagate unimpeded to numerous observer locations. To facilitate direct comparison between in-tunnel and free-air simulation results, the same mesh distribution and resolution were maintained in both setups within a sizeable domain surrounding the GLBC model. The Reynolds number (based on mean aerodynamic chord), Re, and Mach number, M, were 4.4×10^6 and 0.2, respectively. The AoA was set at 9°, representative of aircraft landing conditions. The aerodynamic data extracted from the free-air simulations were used to assess directly the effects of tunnel walls on surface pressure distribution, lift, drag, and pitching moment coefficients.

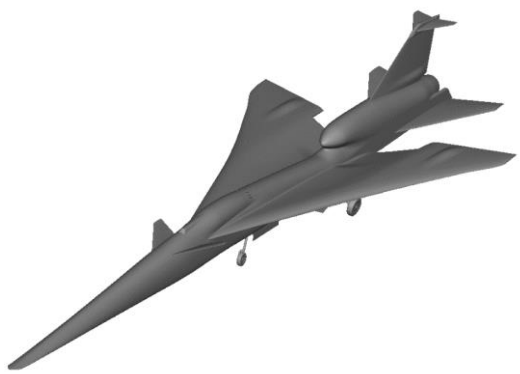

Fig. 14 Close-up image of GLBC CAD model with flaps deflected 30° and landing gear deployed (landing condition) in a free-air setup.

Because experimental noise measurements for the GLBC model do not exist, the acoustic analysis relied solely on the simulated (synthetic) pressure field. Not constrained by the 14x22 tunnel, a synthetic array of 800 phased microphones was developed and used for precise resolution and ranking of prominent airframe noise sources for the 15%-scale GLBC model. The nonredundant array pattern comprised three nested, multi-arm, spiral subarrays targeting different frequency ranges. More details about the array design can be found in Ref. [14]. The array was scaled to obtain the desired array resolution based on its relative distance to the aircraft. A hyperbolic tangent-based shading algorithm was employed during beamforming to improve array resolution while preserving a good signal-to-noise-ratio (SNR) for all frequencies of interest (about 10 dB at low frequencies and at least 16 dB at mid to high frequencies). The array was placed in the overhead position (directly underneath the GLBC) in the flyover direction and at 32.5° in the sideline. Schematics of the array position relative to the model and the microphone pattern are shown in Fig. 15. The array was designed for an operational frequency range of approximately 1.0 kHz to 50 kHz (0.15 kHz to 7.5 kHz full-scale). The array has a diameter of 13.12 ft (4 m) and was placed 17.5 ft (5.334 m) from the model, corresponding to the physical distance between the tunnel centerline and a sideline array when the 14x22 is operated in an open-jet mode [15]. Although not used in the present study, synthetic array data were also generated for the 97-microphone array typically used in this tunnel to allow direct validation of the simulated results when experimental data become available.

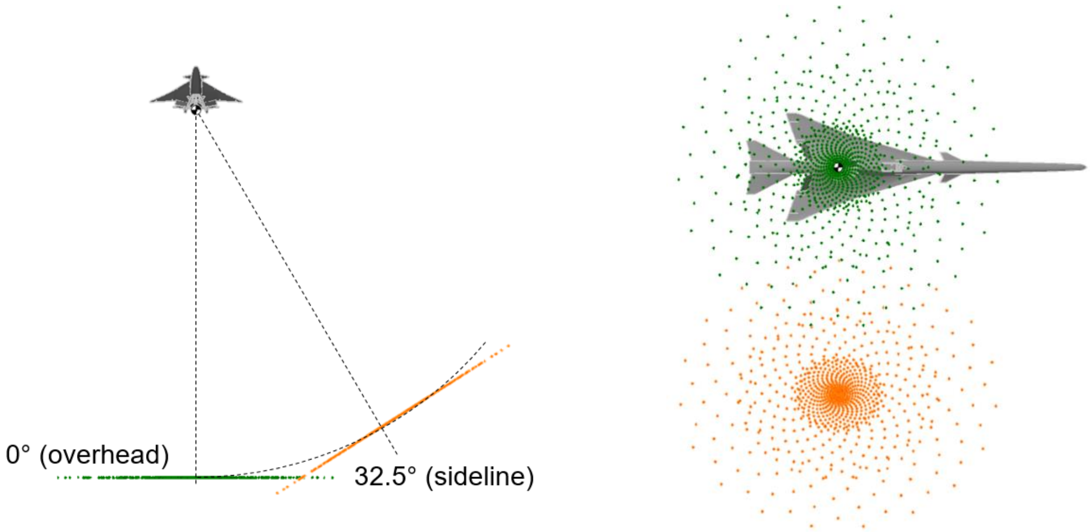

a) Array positions b) Microphone patterns

Fig. 15 Phased microphone array positions and configurations. Green dots represent microphones in the overhead array and orange dots signify microphones in the sideline array.

An acoustic analogy approach based on the Ffowcs-Williams and Hawkings (FW-H) formulation [16] was used to propagate the computed nearfield pressure fluctuations to the array microphone locations. For all simulated configurations, data collected on a tailored FW-H permeable surface were used as input to calculate the far-field pressure records at the two array locations. For Flap30-LGon, the computed unsteady pressure field on the GLBC solid surface was also used as input. The permeable data surface is shown in Fig. 16, including a series of end caps used to reduce the effects of hydrodynamic fluctuations exiting the surface. Notice that, contrary to permeable data surfaces used for conventional subsonic aircraft, the present surface encloses a large volume above the model. This was done to properly contain the highly interactive, complex, off-surface vortical flow field that develops on the upper surface of the model. Obviously, the need to include such a large volume within the permeable data surface substantially increased the computation cost of the simulations, even at the lower resolution levels. The synthetic microphone array pressure records contain nearly 0.065 s of simulated physical time (0.4 s in full-scale).

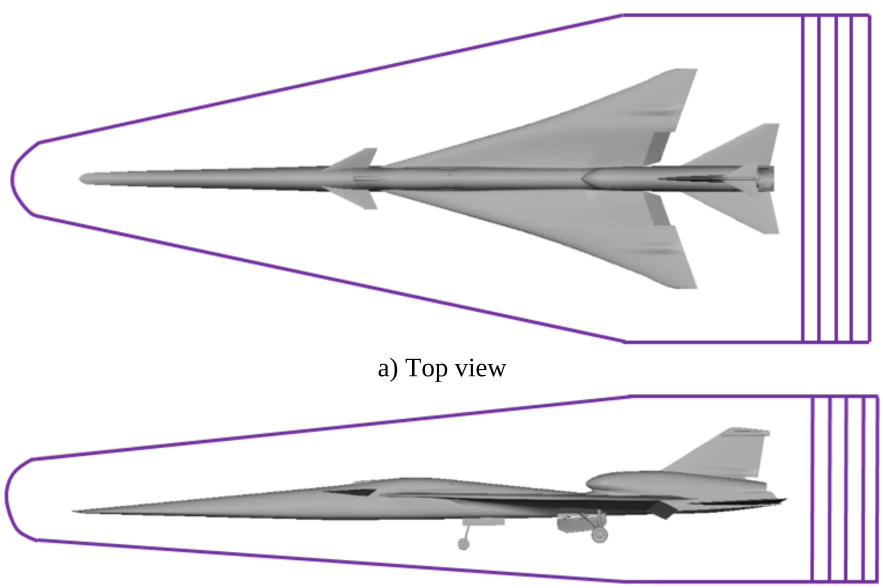

a) Top view

b) Side view

Fig. 16 GLBC model with permeable FW-H data surface drawn in purple lines (from Ref. [12]).

V. Results

Validation of the predicted aerodynamic trends via comparison of measured forces and steady surface pressure with in-tunnel simulated results is presented first. Also included in the comparison are computed aerodynamic data from free-air simulations to highlight the effects of tunnel walls and model support. The aerodynamics section is followed by presentation of acoustic results based on detailed analysis of the synthetic microphone array data.

A. Aerodynamic Comparison

Predicted aerodynamic forces are compared with measured data for the Flap0-LGoff configuration in Fig. 17. In-tunnel predicted results (CFD-WT) obtained from coarse and medium spatial resolution simulations conducted at AoAs of 0.09°, 3.07°, 6.06°, and 9.05°, which correspond to the tested conditions and cover a moderate AoA range, are presented. Due to its importance, the case with AoA = 9.05° was simulated at an additional finer resolution level. Overall, good agreement between predicted and measured data for lift, drag, and pitching moment coefficients was achieved even at the lower resolution level executed. The agreement with measured values improved slightly with increased resolution, indicating that results were near convergence. The drag polar presented in Fig. 17d indicates that the largest discrepancy occurs at AoA = 0°, near the minimum drag point. The lift, drag, and pitching moment coefficients obtained from the free-air simulations (CFD-FA) conducted at AoA = 9° are also plotted in Fig. 17. In general, the predicted free-air values show good convergence with increased resolution and fall within a few percentage points of the in-tunnel results. The close agreement between a) the computed forces obtained from the two simulation setups and b) the predicted and measured values, clearly demonstrates that, as tested in the 14x22, tunnel wall and model support effects on the model aerodynamic characteristics are negligible. This finding fully corroborates the insignificant impact that application of tunnel-wall corrections had on the 14x22 measurements and the appropriateness of using the uncorrected aerodynamic data for validating the simulated results, as stated in section IV.A.

Time-averaged pressure distributions on the model port wing for the lowest AoAs simulated are shown in Fig. 18. For AoA = 0.09° and 3.07° (Figs. 18a and 18b, respectively), good agreement between predicted and measured pressures is observed. Notice that the predicted pressures on the bottom surface of the wing show a small but constant offset from the measured values. As described in Ref. [11], extraction of reference velocity and pressure from the in-tunnel simulations in a manner that would duplicate the calibrated reference conditions defined during the 14x22 GLBC test is not a simple task. Therefore, small errors in the reference conditions extracted from the wind-tunnel simulations are manifested as noticeable deviations, especially when normalizing small (close to zero) forces or pressures. The aforementioned discrepancy between predicted and measured values near the minimum drag point in Fig. 17d may be affected by errors in the reference velocity and pressure. At AoA = 6.06° (Fig. 18c), the measured pressures show the presence of a mild and broad suction peak – induced by the primary leading-edge vortex – centered around the 128-inch station. In contrast, the predicted pressure distribution shows the vortex suction to occur much farther downstream, at the 138-inch station that is close to the wing trailing edge. Notice that the computed pressures are well converged even at the coarse resolution level. The surface pressures at AoA = 9.05° are shown in Fig. 19. Observe from Fig. 19a that the measured pressures indicate a well-defined, vortex-induced suction peak at the 120-inch station. At this AoA, the predicted vortex suction peak appears downstream of the measured peak, moves toward the wing leading edge and gains strength with increased spatial resolution. Unfortunately, the measured pressures lack sufficient resolution to determine the exact shape and location of this peak. However, regarding vortex location, it is highly unlikely that further grid refinement would have yielded better agreement, highlighting the challenges associated with predicting leading-edge flow separation on smooth surfaces. A quick glance at Fig. 19a may also give the impression that simulated pressures substantially overpredicted the measured peak at the wing leading edge. A close-up view of the predicted pressures at the wing leading edge (Fig. 19b) depicts a rather complex distribution. Notice that the synthetic leading-edge suction peak occurs on the wing bottom surface and is followed by a rapid deceleration of the flow before reaching the top surface. Again, the measured pressures lack the necessary spatial resolution to provide better insight on the nature of the leading-edge pressure distribution experienced by the GLBC model during the 14x22 test. More importantly, we must point out that the boundary layers developed at the leading edges of the model were, in all likelihood, thin and laminar before being tripped downstream of the edge. In contrast, the present simulations were performed in a fully turbulent mode [11]. Certainly, the state of the flow at the wing leading edge has a significant effect on boundary layer separation, shear layer rollup, and the resulting formation of primary and secondary longitudinal vortices. Although the laminar flow extent at the leading edge, the effects of trip dots, and the ensuing boundary layer transition could have been partially modeled in our simulations, the extra effort was beyond the scope of the present study and was, thus, not pursued. Predicted pressure distributions obtained from free-air simulations at AoA = 9° are compared to measured values in Fig. 20. Here, the synthetic vortex-induced suction peak is somewhat diffused and occurs slightly downstream of the in-tunnel predictions depicted in Fig. 19a. Nevertheless, the overall trends of enhanced vortex suction and upstream movement of the peak with increased resolution remain very similar to the trends observed for the in-tunnel simulations.

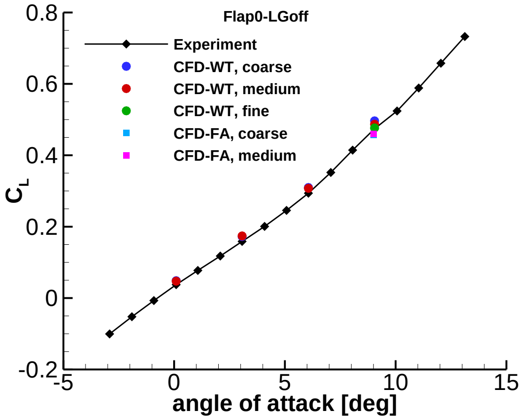

a) Lift coefficient

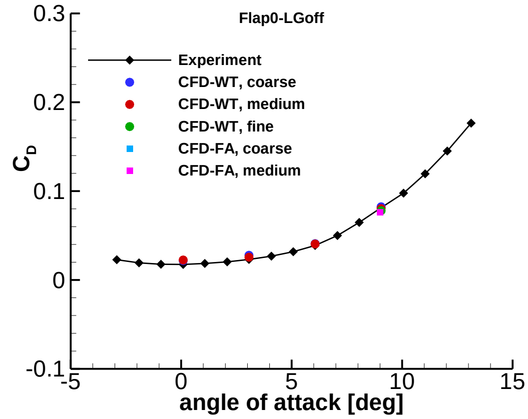

b) Drag coefficient

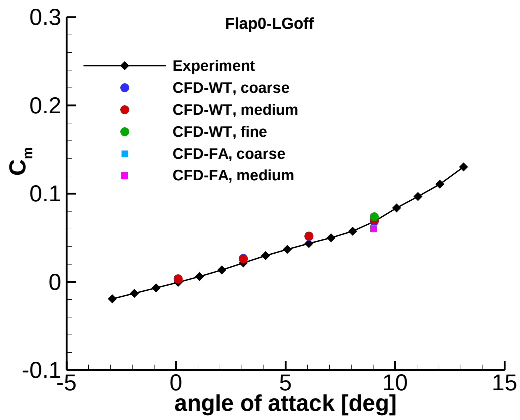

c) Pitching moment coefficient

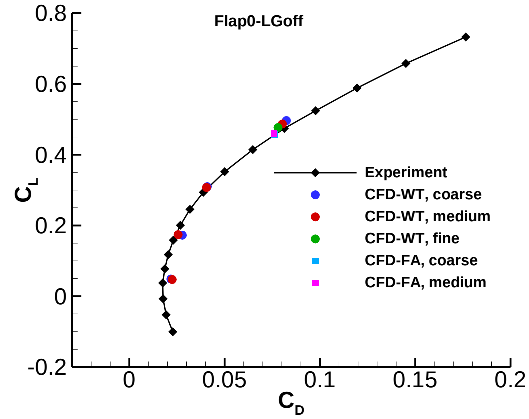

d) Drag polar

Fig. 17 Lift, drag, and pitching moment of GLBC model for Flap0-LGoff configuration.

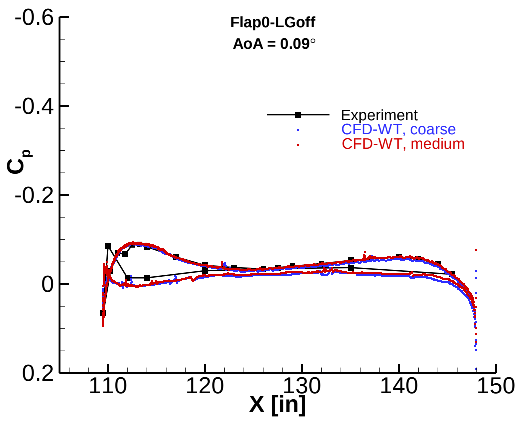

a) AoA = 0.09°

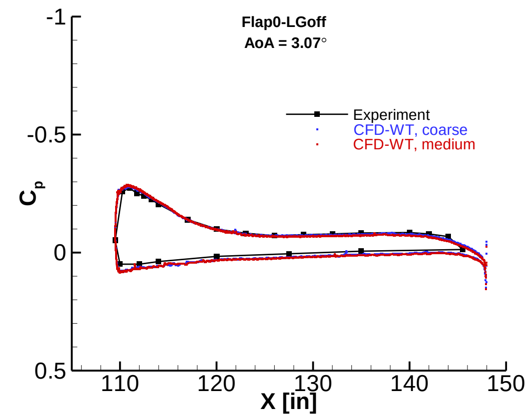

b) AoA = 3.07°

Fig. 18 Streamwise pressure distributions of GLBC for Flap0-LGoff configuration.

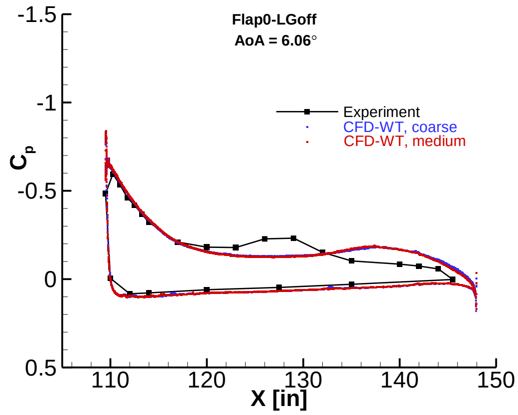

c) AoA = 6.06°

Fig. 18 Concluded.

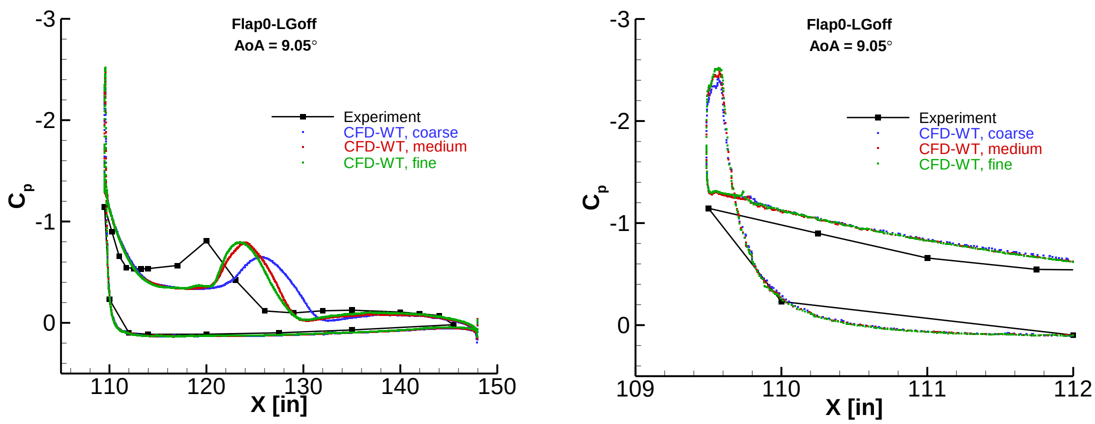

a) AoA = 9.05°

b) AoA = 9.05°, wing leading edge

Fig. 19 Streamwise pressure distributions of GLBC for Flap0-LGoff configuration at AoA = 9.05°.

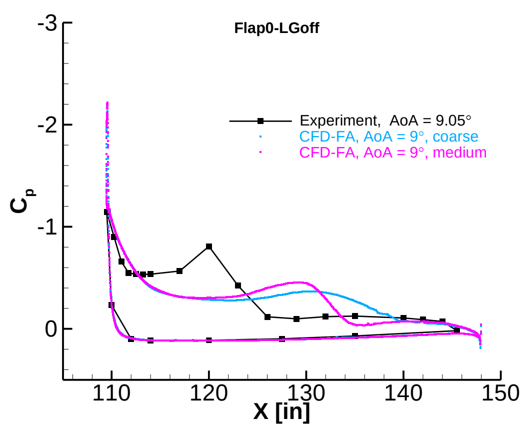

Fig. 20 Streamwise pressure distributions from free-air simulations of GLBC for Flap0-LGoff at AoA = 9°.

Simulated lift, drag, and pitching moment coefficients for the Flap30-LGon configuration at AoAs of 5.88° and 8.9° are compared to wind tunnel measurements in Fig. 21. Also included in these plots are the computed coefficients from free-air simulations conducted at AoA = 9°. The results from the two simulation setups are in good agreement with each other as well as with measurement. However, both in-tunnel and free-air results modestly underpredict the measured lift and drag coefficients. Despite this underprediction, when viewed in the drag polar of Fig. 21d, the computed fine-resolution lift and drag coefficients display the same dependency as the measured data and fall on the same curve.

Surface pressure distributions for Flap30-LGon obtained from the in-tunnel simulations at AoA of 5.88° and 8.9° are depicted in Fig. 22. At the lower AoA (Fig. 22a), the computed data indicate that the pressures are fully converged, even at the coarse resolution level. Except for the broad and mild (vortex-induced) pressure rise apparent at midchord, the predicted pressures are in very good agreement with measured values. As noted for the cruise configuration (Fig. 18c), the absence of vortex suction depends more on the state of the boundary layer on the upper surface and the inherent difficulties with capturing flow separation on smooth surfaces than on the insufficient spatial resolution. The predicted pressure distributions at AoA = 8.9° (Fig. 22b) display differences with measured values similar to those observed for the cruise configuration (Fig. 19a), with vortex-induced suction occurring farther downstream of the wing leading edge than indicated by measurements. Marked improvements in vortex suction levels and peak location are observed with increased spatial resolution. For the finest resolution executed, the difference in positions between predicted and measured vortex suction peaks is less than 4 inches, or about 8% of the local chord length. As the trends in Fig. 22b indicate, further improvement in leading-edge vortex location could have been realized had we used an even finer resolution level. However, as the grid size and other simulation attributes provided in Ref. [11] illustrate, such an attempt would have been enormously challenging in terms of computational resources and cost. Corresponding predicted Flap30-LGon pressure distributions extracted from the free-air simulations at AoA = 9° are presented in Fig. 23. With minor differences, the computed pressures depict trends very similar to those observed for in-tunnel data (Fig. 22b), reinforcing the fact that the tunnel walls and model support have negligible effects on the GLBC aerodynamics. Although not shown, the computed pressure distribution at the wing leading edge for the Flap30-LGon configuration was similar to those presented in Fig. 19b.

The predicted data presented in Figs. 17-23 clearly demonstrated the efficacy of the simulation in capturing the critical aspects of the aerodynamic characteristics of this aircraft and allowed us to proceed with the companion acoustic analysis.

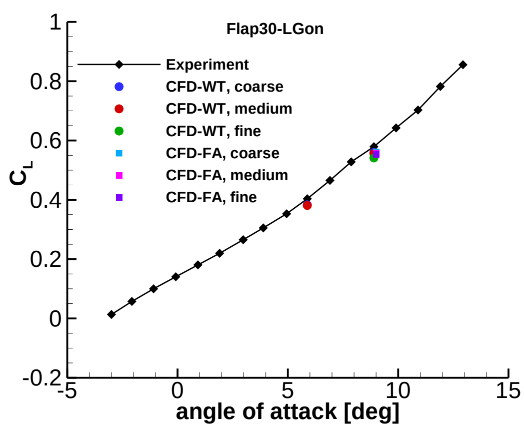

a) Lift coefficient

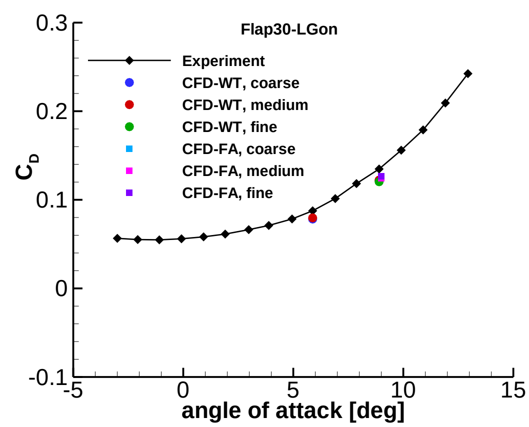

b) Drag coefficient

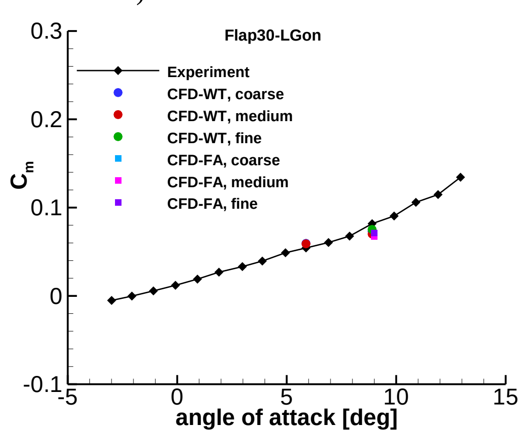

c) Pitching moment coefficient

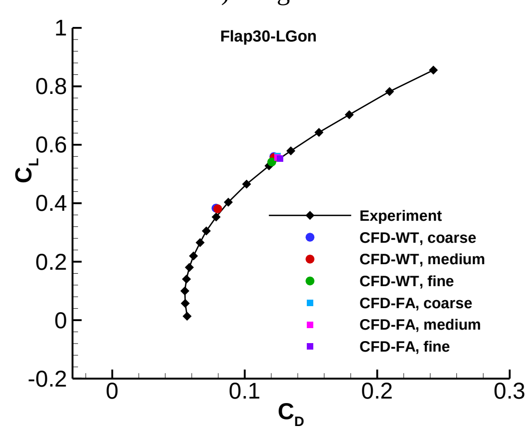

d) Drag polar

Fig. 21 Lift, drag, and pitching moment of GLBC model for Flap30-LGon configuration.

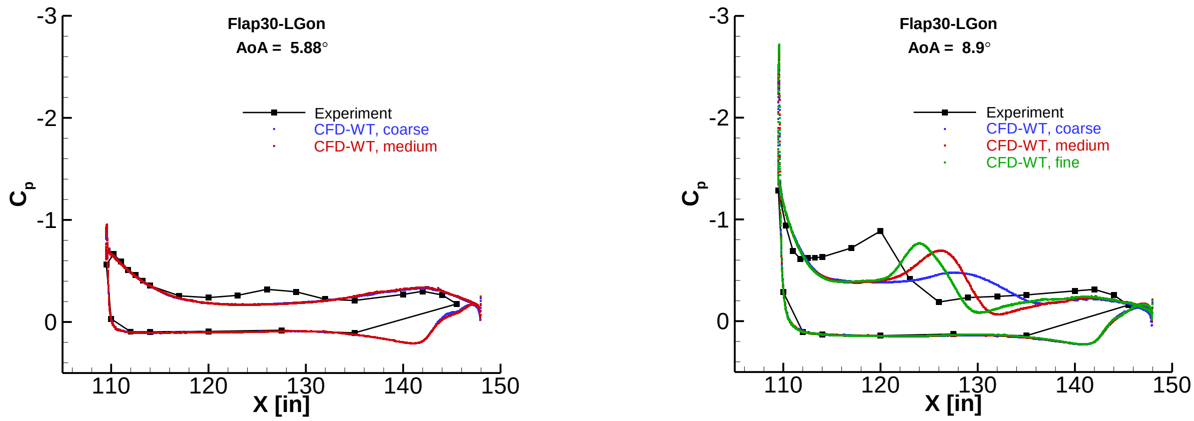

a) AoA = 5.88° b) AoA = 8.9°

Fig. 22 Streamwise pressure distribution of GLBC model for Flap30-LGon configuration.

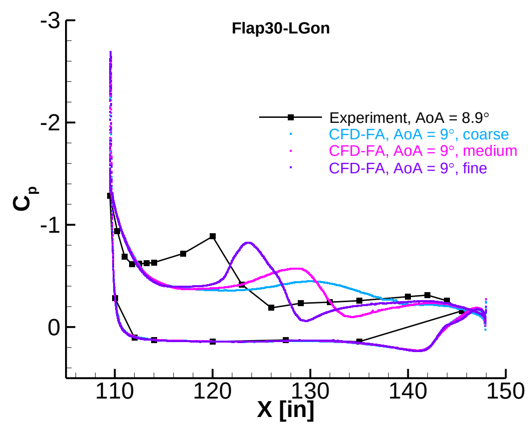

Fig. 23 Streamwise pressure distributions from free-air simulations of GLBC for Flap30-LGon configuration at AoA = 9°.

B. Acoustic Analysis

Given the lack of experimental information on airframe noise sources for commercial supersonic transports, we have relied exclusively on synthetic array data to acquire initial insights into the underlying physical phenomena. Microphone arrays are an ideal tool for a thorough examination of primary and secondary airframe noise sources, determination of their relative strengths, and their contribution to the total far-field noise levels. To this end, the present synthetic phased microphone array was implemented with precise resolution and ranking of primary and secondary noise sources in mind.

1. Synthetic Array Data Processing and Integration Regions

The simulated pressure records were beamformed in the frequency domain and post-processed using the CLEAN technique [17] as implemented in AVEC's phased array software suite [18]. Diagonal removal was applied to exclude potential contributions from uncorrelated noise. The beamform (source localization) maps were generated on a 6.3 m by 3 m planar grid, with a resolution of 0.02 m in both directions, covering the entire aircraft. After several iterations, the mid distance between the GLBC landing gear wheels and wing was determined to be the best compromise for placement of the planar grid. In this position, nearly all of the airframe sources are close to the selected plane without affecting significantly the integrated levels. The location of the chosen beamforming plane is shown in Fig. 24 and its extent is displayed in Fig. 25. Integration results were computed from CLEAN maps obtained with "zero-resolution," thus avoiding the need for normalization. For visualization purposes, however, the CLEAN acoustic maps presented here were generated using an artificial resolution of 0.1 m. The narrowband beamform maps were generated using a bandwidth of 350 Hz and a 15 dB cutoff range.

Fig. 24 Extent and position of beamforming plane. Grid resolution: 0.02 m.

To generate far-field spectra, the CLEAN beamform maps were integrated with a 10 dB cutoff. Carefully oriented integration regions were devised to extract contributions from various sections of the aircraft. These integration regions are shown in Fig. 25. Notice that the "Canards" integration region includes the juncture between the fuselage and wing apex, and thus may contain noise sources other than the canards. The integrated spectrum for the "Whole" grid that covers the entire scanning plane was also computed with a 15 dB cutoff to include the contributions from all relevant sources to the overall noise signature. The summation of contributions from all subregions (based on p^2) is termed "Sum" and is used to illustrate the total airframe noise produced by GLBC. Unless stated otherwise, all spectra presented in the acoustic analysis correspond to the overhead position.

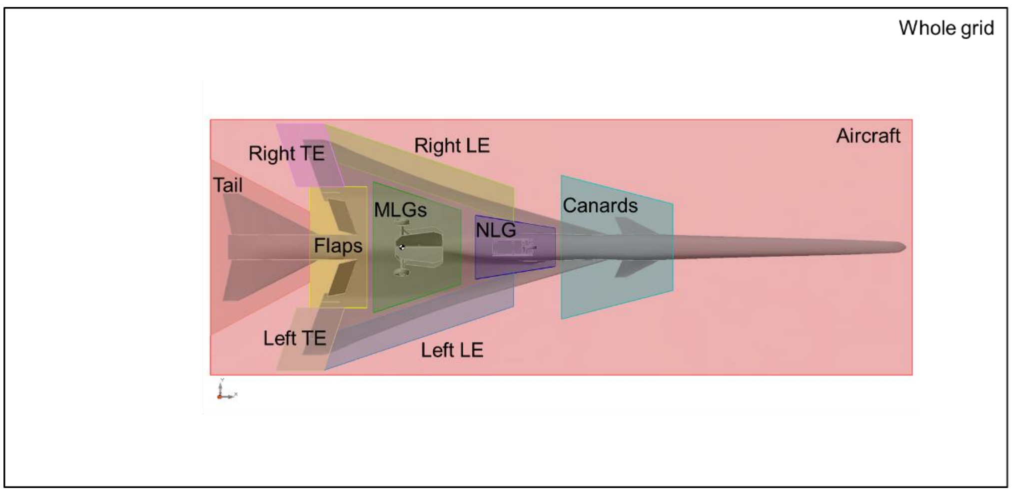

Fig. 25 Regions used to calculate integrated far-field noise spectra.

2. Effects of End Caps and Spatial Resolution

As illustrated in Ref. [11], the large-scale, longitudinal vortices generated by the GLBC canards and those produced at the wing leading edges persist for long distances downstream of the aircraft. Passage of such coherent structures through the exit plane of the permeable data surface is problematic, and in most cases results in generation of numerical sound sources that are detrimental to the accuracy of predicted noise levels. As shown in Fig. 16, to partially circumvent this problem, multiple end caps were devised and applied to diminish significantly the contribution of these nonphysical noise sources through end-cap averaging. Nevertheless, a posteriori checks of the effectiveness of this cap averaging strategy is always recommended. For this reason, the extent of the planar "Whole" grid used for beamforming was chosen to contain all potential noise sources, whether physical or numerical.

Although five end caps were used, examination of the beamform maps revealed the presence of strong numerical sources at the exit plane of the permeable data surface. Sample beamform maps from the medium resolution simulation of the Flap30-LGon configuration are shown in Fig. 26. At low to moderate frequencies (Fig. 26a), due to dominance of the landing gear and flap sources, the numerical sources at the end caps region appear weak and thus do not contribute significantly to the far-field noise levels. However, at frequencies above 13 kHz to 14 kHz (Fig. 26b), the end cap numerical sources become the most dominant by far. Closer examination of the CLEAN maps and contour levels over a wide frequency range revealed that the numerical sources maintain a nearly constant strength, as can be observed when comparing the maps in Figs. 26a and 26b. For Flap0-Lgoff, which represents the quietest configuration, contribution of the numerical sources to the overall noise levels becomes substantial at much lower frequencies (Fig. 27a); at the mid-frequency range (Fig. 27b), they appear as the most prominent sources in the beamform maps. One way to circumvent the numerical sources is to ignore the contribution of the end caps during the FW-H propagation step when synthetic pressure records are generated at the array microphone locations. Beamform maps excluding end cap contributions are depicted in Figs. 28 and 29. As evidenced in these sample maps, the nonphysical sources downstream of the GLBC tail disappear altogether over the entire frequency range of interest. The central question of whether, and by how much, the physical noise sources are affected by ignoring contributions from the end caps is addressed next via examination of the integrated far-field power spectral density (PSD) results.

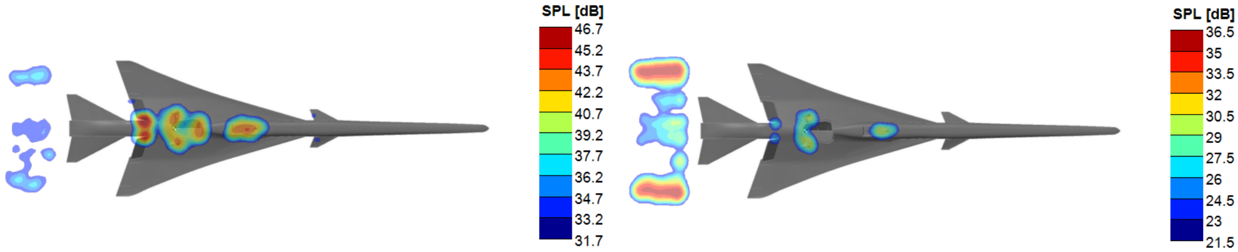

a) 7,698 Hz b) 17,845 Hz

Fig. 26 Effect of end caps on CLEAN maps from medium resolution simulation of Flap30-LGon (landing) configuration.

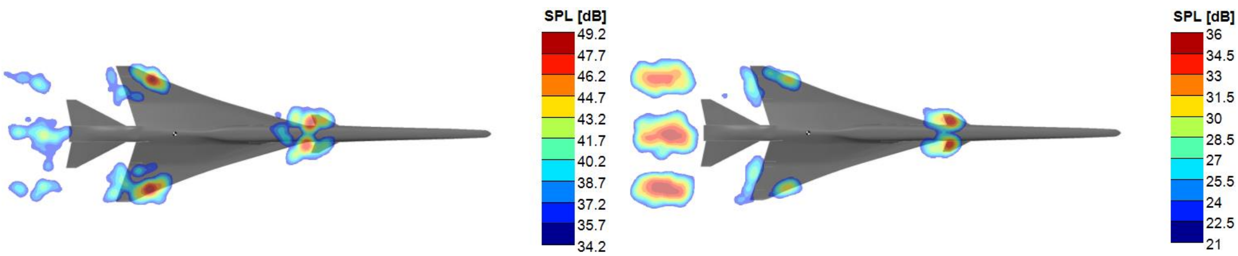

a) 2,799 Hz b) 7,698 Hz

Fig. 27 Effect of end caps on CLEAN maps from medium resolution simulation of Flap0-LGoff (cruise) configuration.

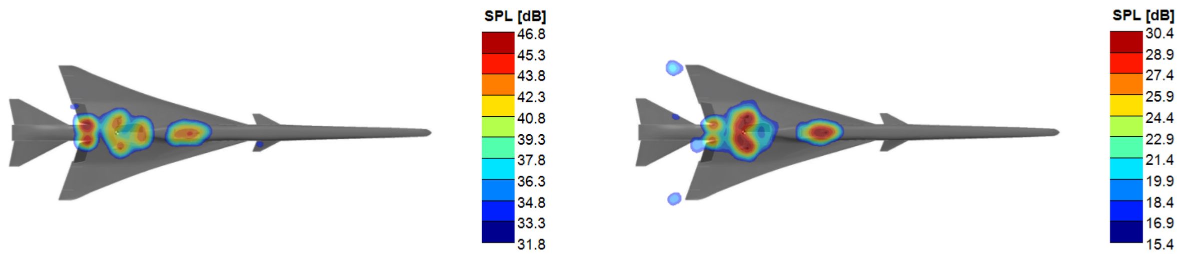

a) 7,698 Hz b) 17,845 Hz

Fig. 28 Effect of end cap removal on CLEAN maps from medium simulation of Flap30-LGon (landing) configuration.

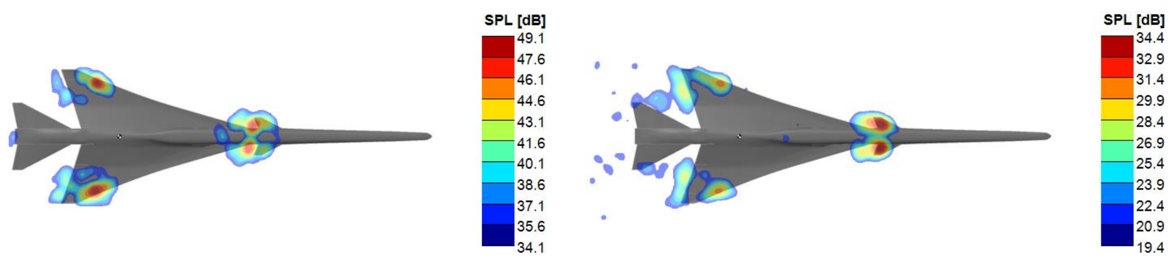

a) 2,799 Hz b) 7,698 Hz

Fig. 29 Effect of end cap removal on CLEAN maps from medium simulation of Flap0-LGoff (cruise) configuration.

The far-field spectra for the Flap30-LGon configuration, obtained from integration of the "Whole grid" region, is presented in Fig. 30a. The PSD results from the permeable data surface with and without contribution from the end caps are plotted. For frequencies up to 4 kHz, the two spectra are nearly identical, indicating that end cap contribution to the far-field noise levels is negligible relative to the contributions from all other airframe sources. Beyond 4 kHz, the difference between the two PSD curves increases gradually until it reaches about 10 dB at frequencies greater than 16 kHz. As will be shown later, for frequencies above 16 kHz to 17 kHz, the accuracy of the noise levels obtained at medium resolution degrades due to insufficient spatial resolution. Plotted in Fig. 30b are the spectra obtained from integration of the "Aircraft" region. Notice that, once the area downstream of the GLBC tail containing the numerical sources is excluded from integration of the CLEAN maps, the same spectrum emerges regardless of whether the end caps were included or excluded. The spectra obtained from the summation "Sum" of all airframe sources are displayed in Fig. 30c. The effect of end caps on noise sources associated with individual airframe components is captured in Fig. 30d, where the spectra obtained for the MLG are used as an example. The results of Figs. 30c and 30d clearly demonstrate that the end caps do not affect the accuracy of the integrated far-field noise spectrum, be it from individual components or from the sum of all sources on the model. Far-field noise spectra obtained from integration of beamform maps with and without end cap contribution for the Flap0-Lgoff configuration (not shown) followed trends similar to those observed in Fig. 30. Thus, unless specified otherwise, only results obtained from permeable data surfaces without end cap contribution are presented herein.

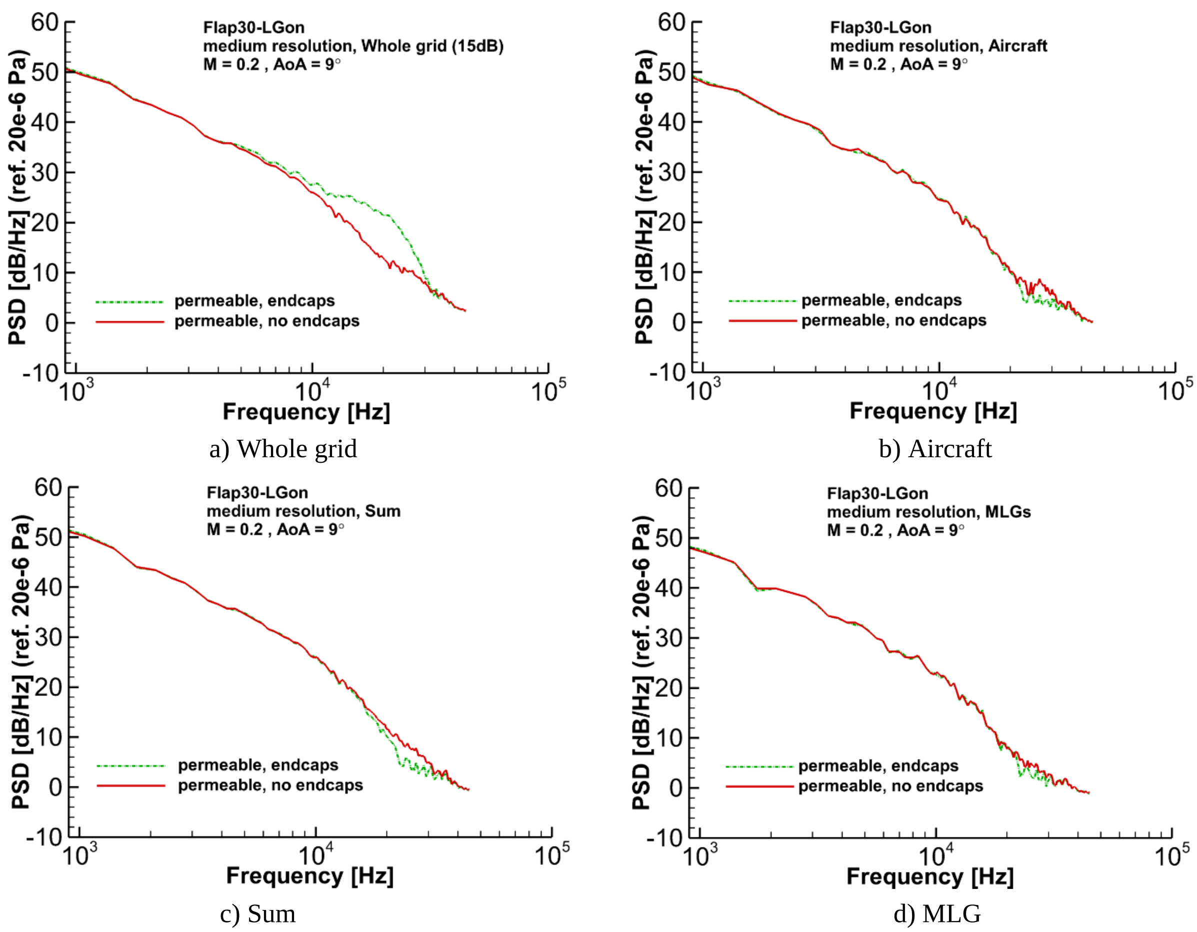

Fig. 30 End cap effect on integrated spectra obtained from medium simulation of Flap30-LGon configuration.

We now examine the effects of spatial resolution on the distribution of sources, their relative strengths, and integrated far-field noise spectra. For this purpose, we consider the Flap30-LGon configuration, which is the most computationally challenging case we studied and the only configuration where simulations at three grid resolution levels were conducted.

CLEAN beamform maps obtained from coarse, medium, and fine spatio-temporal resolution simulations are shown in Fig. 31 at various frequencies within a broad range. At a low frequency of 3.85 kHz (Fig. 31a), all maps depict fairly converged source distributions and strengths for the primary noise sources – MLG and flaps. Even the levels for weaker sources – NLG, canards, and wing leading edges – show relatively good agreement among the maps. As shown in Fig. 31b, this good agreement extended to a moderate frequency of ~7.7 kHz for the most dominant sources, including flap inboard tips, MLG, and NLG. Notice that additional sources, such as those originating from flap outboard tips, emerge more clearly in the maps as resolution is increased. However, the distribution and strength of the sources originating from the canards and wing leading edges keep changing and do not display the typical convergence trends one would anticipate from increased spatial resolution. As illustrated in Ref. [11], this behavior is mostly due to the inherent difficulties in capturing leading edge separation on smooth surfaces that leads to shear layer roll-up and formation of large-scale longitudinal vortices. With increased resolution, even the slightest chordwise movement of the separation point causes vortex meandering that results in gradual, nonmonotonic convergence of the flow field on the upper surfaces of the GLBC wing and canards [11]. Meandering of the vortices, which could cause these structures to either move closer to the leading edges or away from the model solid surfaces, may have a noticeable impact on the magnitude and distribution of the resultant noise sources. Beyond 8 kHz, the maps obtained from coarse resolution results show a gradual degradation in the accuracy of the predicted noise levels caused by insufficient spatial resolution (Fig. 31c). Beyond 15 kHz (Fig. 31d), coarse simulation maps reveal a low SNR, culminating in the appearance of various numerical sources that contaminate the integrated spectra. Although these numerical sources generally disappeared at medium resolution, even this level of spatio-temporal resolution was insufficient to accurately predict the peak level at a frequency of about 17.8 kHz (Fig. 31d). However, comparison of maps from medium and fine resolution simulations at even higher frequencies (not shown) revealed that, despite an underprediction in spectral levels, medium resolution maps correctly identified the appropriate airframe sources and their relative strengths.

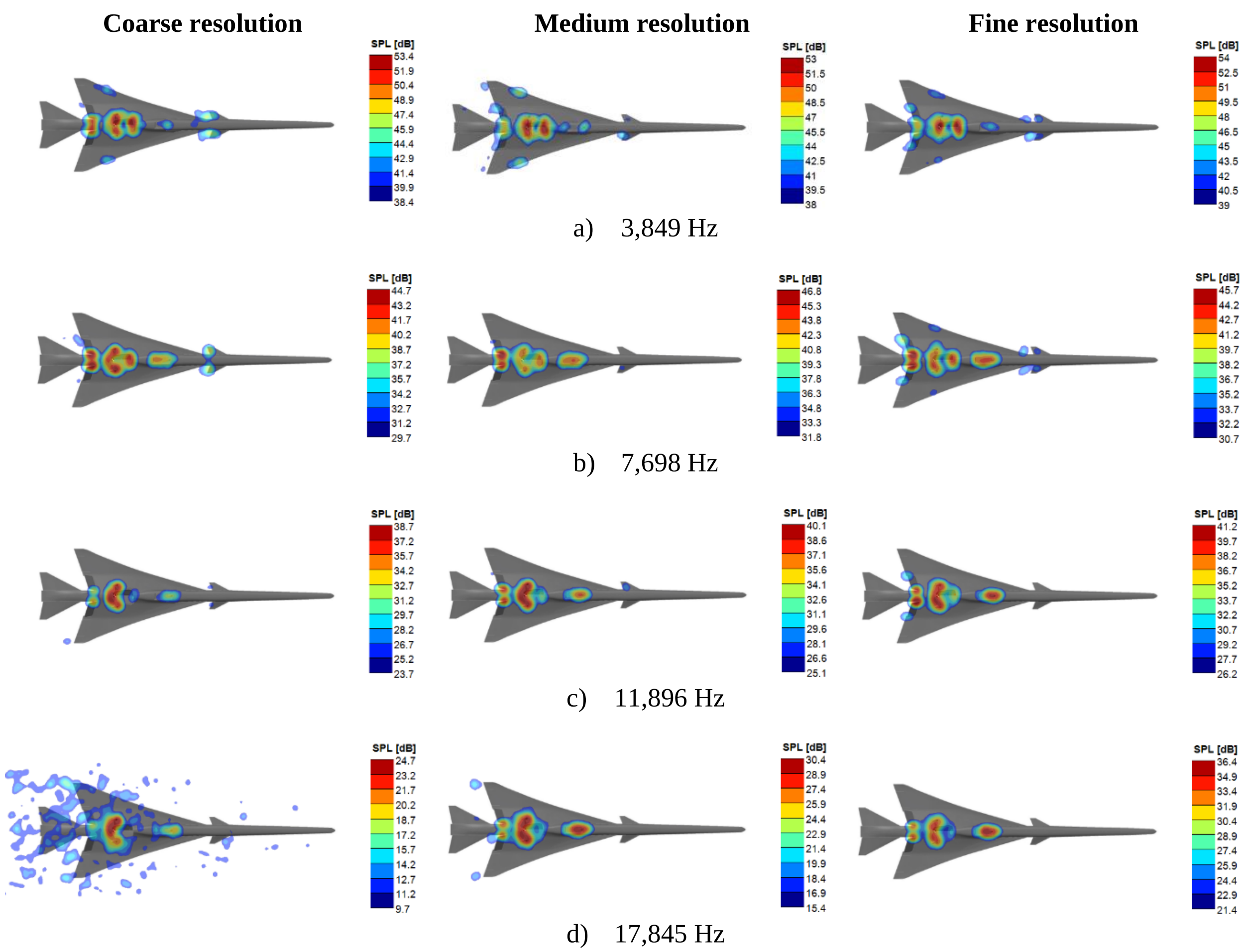

Fig. 31 Spatial resolution effects on CLEAN maps of Flap30-LGon configuration.

Convergence of the Flap30-LGon far-field noise spectra with spatial resolution is shown in Fig. 32. In this figure, spectra from summation ("Sum") of all sources and for landing gear and flap components are presented for the three simulated spatial resolution levels. For frequencies below 18 kHz, the spectra of Fig. 32 indicate that, on both component and total noise levels, the medium resolution simulation produced results that are within 2–3 dB of those obtained from the much more computationally expensive fine resolution simulation. Therefore, the medium resolution grid was selected to conduct most of the acoustic analysis for the GLBC model.

Far-field spectra obtained from integration of the Canards and Left LE regions are shown in Fig. 33. Unlike the spectra presented in Fig. 32, where the levels were well converged below 10 kHz, the spectra for the sources in the Canards and Left LE regions depict a nonmonotonic, slow convergence of the noise levels with increased resolution. This behavior is similar to that observed in the aerodynamic data for the leading-edge vortices reported in Ref. [11]. The trends captured in the plots of Fig. 33 do not provide a clear indication of the appropriate spatial resolution at which fairly converged noise levels for sources below 10 kHz should be apparent. This convergence behavior, which seems unique to swept, low aspect ratio wings typical of supersonic aircraft, may be affected also by the significant difference in noise amplitude between secondary (canards, leading edges, and tail) and primary noise sources (landing gear and flaps). Because the SNR of the array is finite, spurious sources appear within the integration cutoff, even after applying CLEAN. The result is a reduction in the accuracy of the integrated spectra for secondary sources at frequencies where their levels are lower than 10 dB from the peak in the beamform maps.

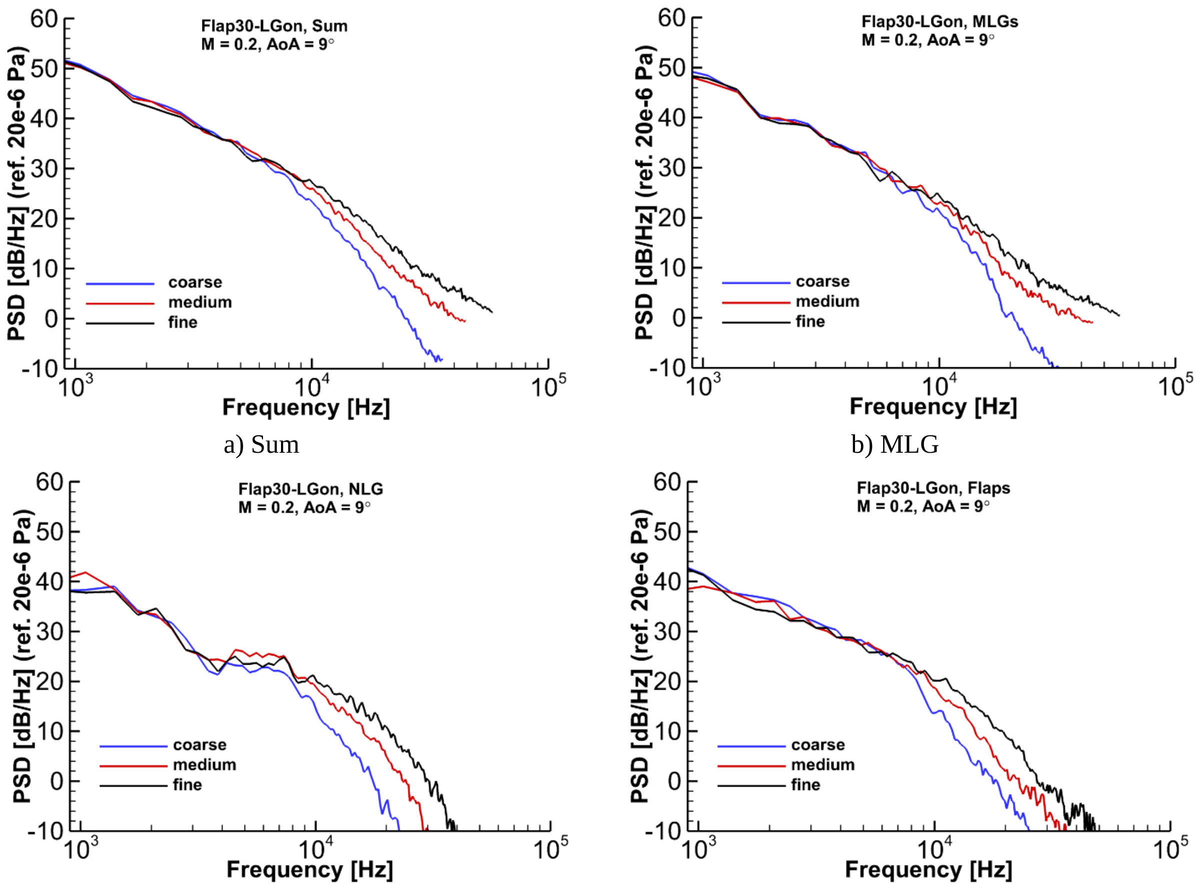

a) Sum b) MLG

c) NLG d) Flaps

Fig. 32 Spatial resolution effects on integrated spectra of Flap30-LGon configuration – landing gear and flaps.

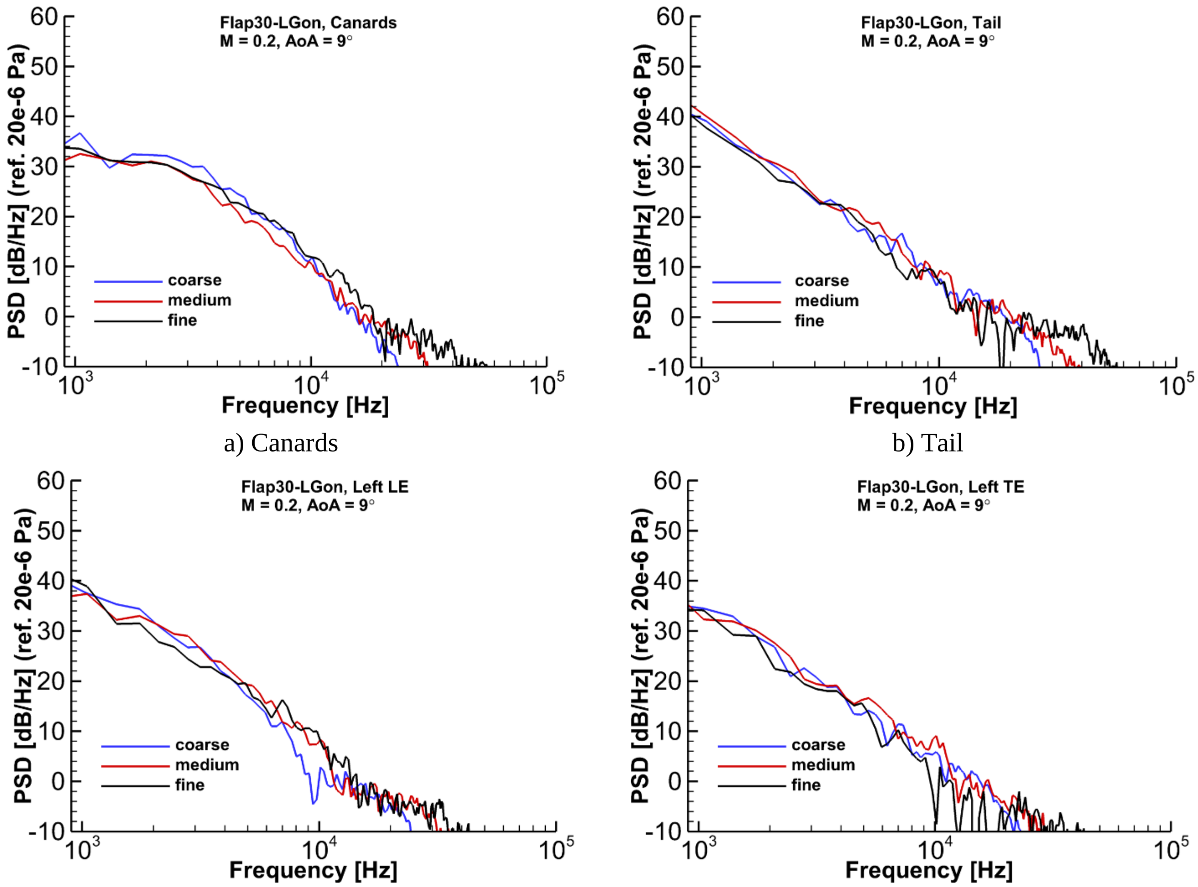

a) Canards b) Tail

c) Left LE d) Left TE

Fig. 33 Spatial resolution effects on integrated spectra of Flap30-LGon configuration – control surfaces and wing.

3. Solid versus Permeable Data Surfaces

For propagation to the far field, the use of aerodynamic data on model solid surfaces as input to FW-H formulations is an attractive approach for various reasons. First, the surface is easily defined without any ambiguity. Second, the collected time-dependent surface pressures are highly accurate since the flow volume in the immediate vicinity of the model surface contains the finest spatio-temporal resolution in the simulation. Third, the simulation has a relatively low cost and a faster solution turnaround time as there is no need to extend the high spatial resolution volume to the permeable surface location. Unfortunately, recent studies have demonstrated that the solid surface FW-H formulation is inadequate for an accurate prediction of far-field noise, especially when shielding effects, quadrupole effects, or cavity noise are prevalent [19–20]. For the GLBC model, single microphone spectra in Ref. [12] clearly showed that the use of solid surface pressures as input data results in significant overprediction of the far-field spectrum over a broad frequency range. We leveraged the present synthetic array data to further examine the differences between solid and permeable data surface results and to gain additional insights into the shortcomings of solid surface spectral results. To do so, we used the medium resolution, unsteady pressure field simulated on the GLBC model surface to produce the pressure records at the array microphone locations.

CLEAN beamform maps generated from solid and permeable data surfaces are depicted in Fig. 34 at various frequencies. At ~3.85 kHz (Fig. 34a), both data surfaces show similar peak levels. As expected, the solid surface map indicates that the MLG and flaps are the prominent airframe sources; it also identifies strong sources inboard of the wing leading edges, toward the trailing edges. The location and distribution of these leading-edge sources suggest that they correspond to the strong, longitudinal vortices that develop on the wing top surface (see Ref. [11] for an aerodynamic analysis of these structures). Evidently, solid surface data cannot account for the shielding effects of the wing. The corresponding permeable surface map displays similar source distribution and strength for the MLG and flaps. In contrast to the solid surface map, however, the location and strength of the wing sources are correctly identified: vortex-generated noise on the wing upper surface propagates laterally to the wing leading-edge region, where it is scattered by the relatively sharp edge before reaching an observer on the ground. Thus, to this observer, the sound would appear to emanate from the wing leading edge. The same trends hold for the maps at ~9.1 kHz, shown in Fig. 34b. At this frequency, both maps show similar peak noise levels and source distributions for MLG, NLG, and flaps, indicating no degradation in signal amplitude as the sound reaches the permeable surface. As observed at the lower frequency, the solid surface map incorrectly depicts vortex-produced sources to reside on the wing lower surface and to possess comparable strength to the MLG and flaps sources. In addition, the map shows the noise generated by the GLBC canards to be of noticeable strength. The corresponding permeable surface map does not show any scattering of the noise produced by the leading-edge vortices, suggesting that the strength of these sources may have fallen below the 15 dB cutoff from the peak levels.

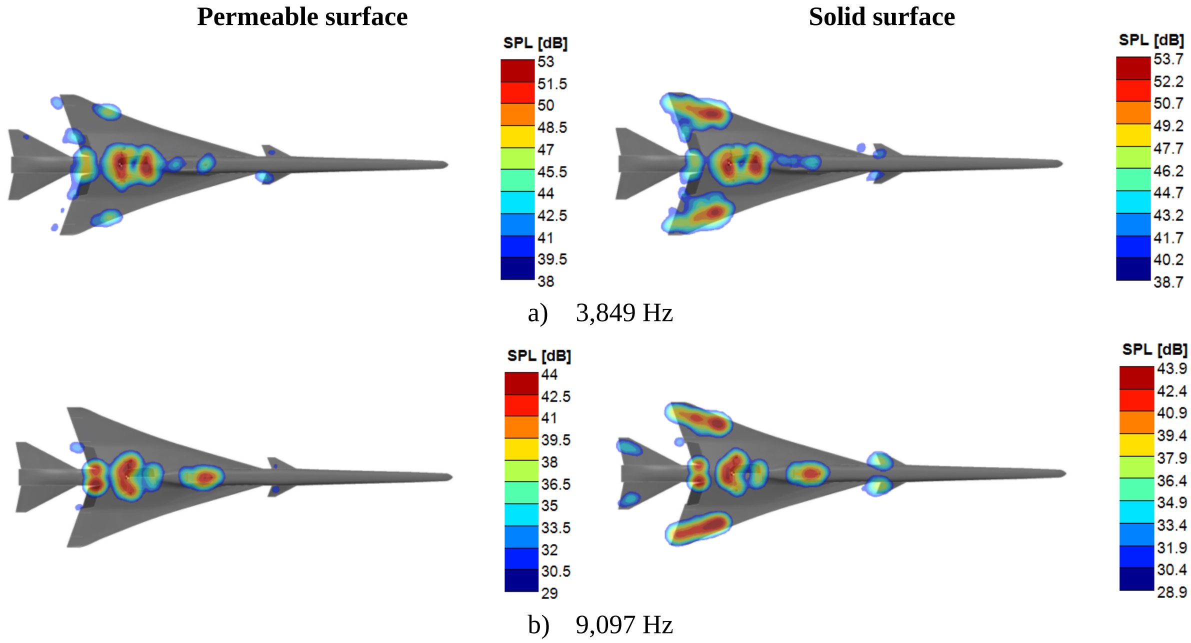

Fig. 34 Effect of data surface on CLEAN maps for Flap30-LGon configuration (medium resolution).

The inadequacy of solid-surface results becomes obvious during examination of integrated far-field spectra. Integrated spectra obtained from the "Sum" of sources as well as MLGs, NLG, and Flaps regions, for both solid and permeable data surfaces, are presented in Fig. 35. For completeness, the permeable results are depicted without and with end cap contribution. Observe from Fig. 35a that the solid surface spectrum substantially overpredicts the total airframe noise being generated by the GLBC model, thus confirming the single microphone results presented in Ref. [12]. However, the spectra shown in Figs. 35b, 35c, and 35d clearly illustrate that both surfaces produce the same noise levels for airframe sources that reside on the model underside, where shielding is not prevalent. In these latter figures, the higher noise levels associated with the solid surface at frequencies above 15 kHz are due to the higher spatio-temporal resolution of the surface pressures or, conversely, correspond to the degradation of higher frequency waves as they propagate through the volume enclosed by the permeable data surface before reaching the surface. To highlight the causes of solid surface overprediction, integrated spectra for the two edge regions on the port (left) side of the model plus the Canards region are presented in Fig. 36. Spectra for the starboard (right) side of the GLBC were similar to those on the port (left) side and thus are not shown here. As was seen in the beamform maps (Fig. 34), the spectra obtained from the solid surface show between 10 dB to 15 dB higher levels than those of the permeable surface. Except for the tail, the overprediction occurs over most of the frequency range of interest. For the canards, the results from the two surfaces agree well for frequencies below 5 kHz. Above this frequency, overprediction of noise by the solid surface data similar to that observed for the wing edges is apparent. The results of this section, plus those presented in Ref. [12], add to the body of evidence on the inadequacy of using solid surface data to predict far-field noise signatures of complex configurations. Accordingly, only results based on permeable surface data were employed to perform our acoustic analysis and draw the appropriate insights and conclusions.

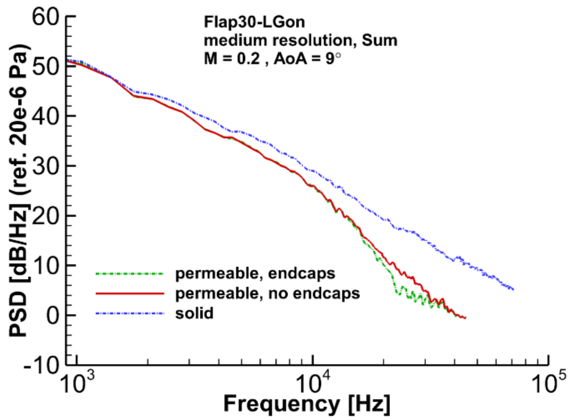

a) Sum

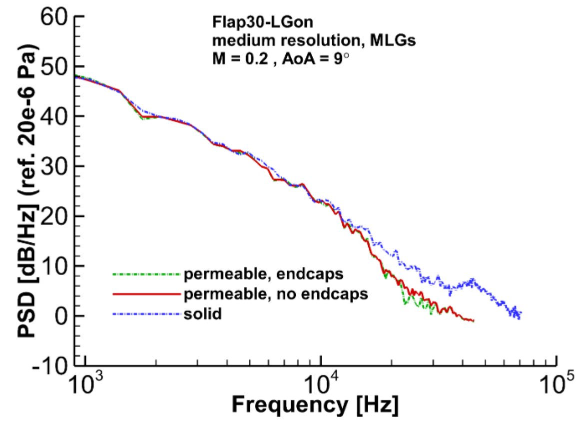

b) MLG

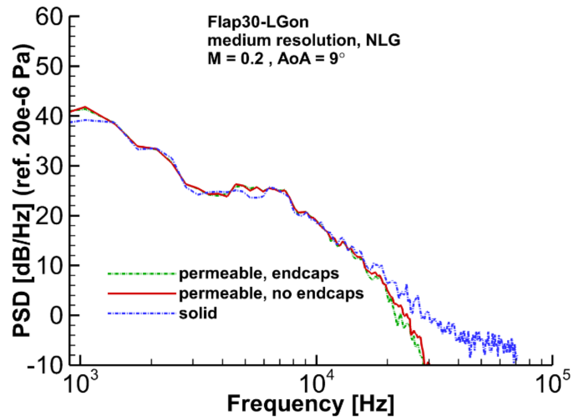

c) NLG

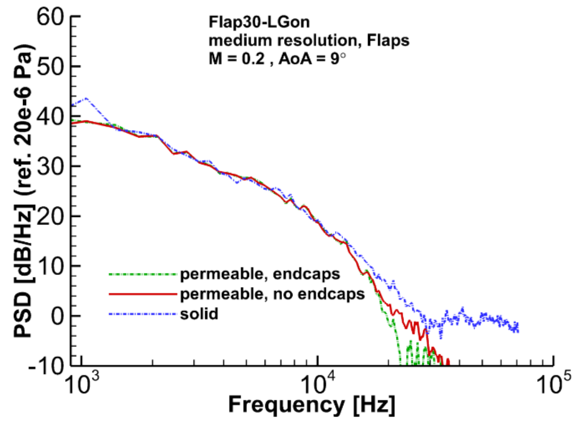

d) Flaps

Fig. 35 Effect of data surface on integrated spectra for Flap30-LGon configuration (medium resolution) – landing gear and flaps.

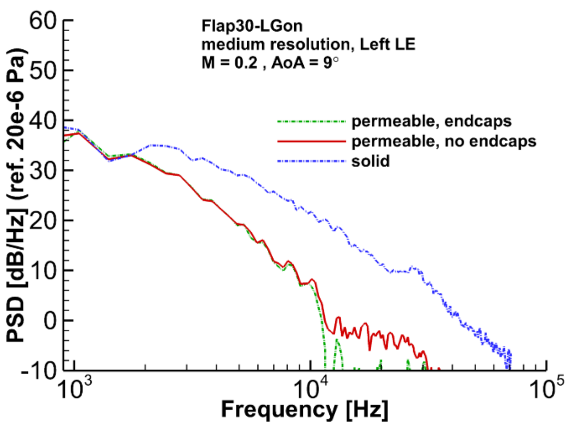

a) Left LE

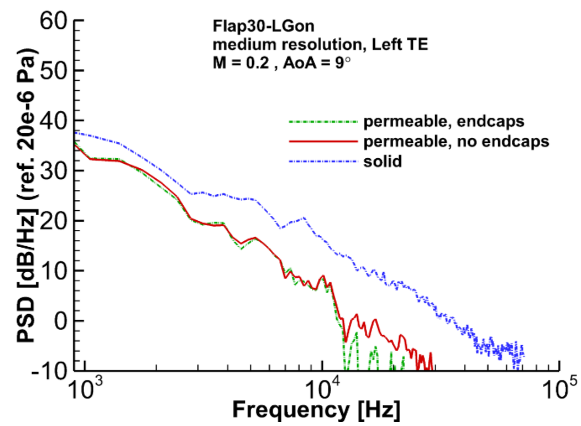

b) Left TE

Fig. 36 Effect of data surface on integrated spectra for Flap30-Lgon configuration (medium resolution) – control surfaces and wing.

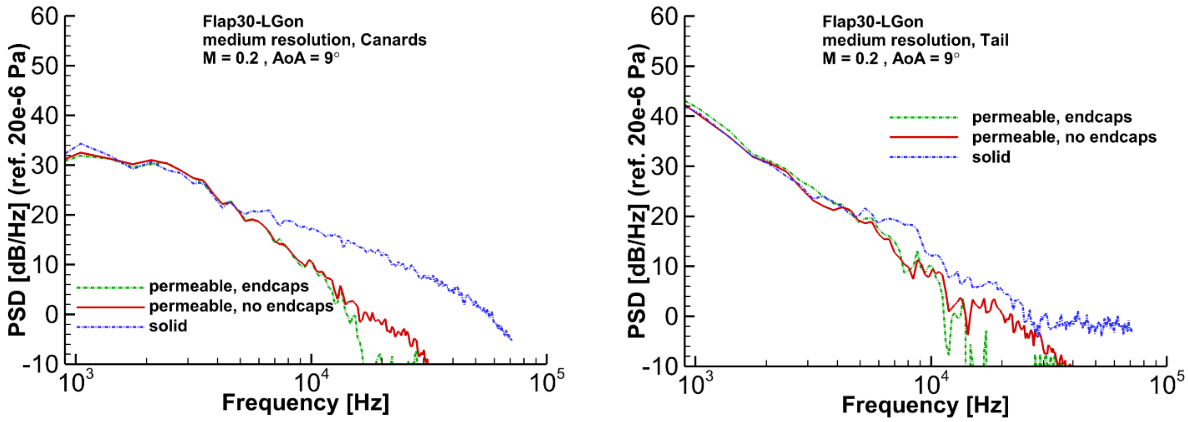

c) Canards d) Tail

Fig. 36 Concluded.

4. Primary and Secondary Airframe Noise Sources

Although the GLBC was not designed to represent a commercial supersonic business jet, much insight can be gained from ranking the airframe noise sources on this model. To this end, we return to the fine resolution CLEAN maps for the Flap30-LGon configuration shown in Fig. 31. A comparison of the maps at the four selected frequencies indicates that the MLG is the dominant source across the entire frequency range, followed by either the NLG or the flaps. The wing leading edges and the canards appear as low-frequency, much weaker airframe sources. The integrated far-field spectral levels associated with the primary airframe noise sources, relative to the model total "Sum" levels, are shown in Fig. 37a. As expected, the MLG is the dominant source, and the fact that its levels are only about 3 dB below the "Sum" suggests that almost 50% of the total GLBC airframe noise is produced by the main gear. Except for frequencies between 2.2 kHz and 7.5 kHz, the NLG and flap sources have similar spectral profiles and contributions to the total noise of the model. Since the undercarriage is very rudimentary, it is not clear whether the present ranking of primary sources would remain once realistic landing gear configurations are considered. Spectra for the important secondary sources are presented in Fig. 37b. Although the canards seem to be the prominent components among the secondary sources, the noise from the wing leading edges would have been comparable had we added together the contributions from the Left LE and Right LE regions. Recall that integrated levels for these components are well below those for the dominant source (MLG) and, therefore, may be less accurate because of the array SNR.

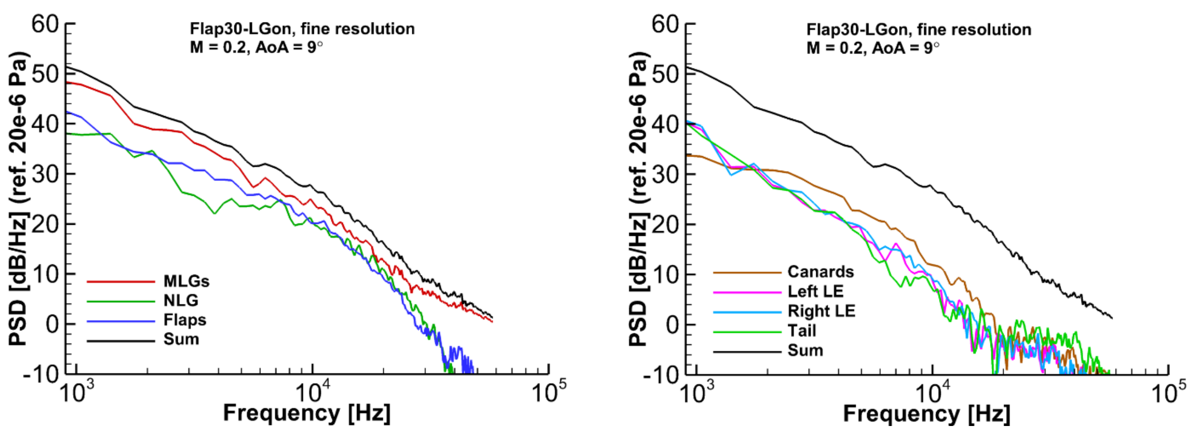

a) Primary b) Secondary

Fig. 37 Integrated spectra for Flap30-LGon (fine resolution) – primary and secondary airframe noise sources.

5. Overhead versus Sideline Far-field Noise Levels

Greater insight into the directivity of airframe noise sources and its effect on far-field noise is necessary for a proper assessment of the impact on community noise and to develop noise certification standards. In Fig. 38, we compare CLEAN maps from flyover and sideline arrays at low and moderate frequencies, obtained from medium resolution results for the Flap30-LGon configuration. The sideline maps feature primary sources with strengths similar to those seen in the corresponding flyover (overhead) maps. However, notice that the sideline maps show the source distributions to be somewhat distorted and slightly off position. This is caused by parallax and the fact that the sources do not reside exactly on the selected grid plane (Fig. 24). The most significant changes occur for the wing leading edge and canard sources. With the sideline array, increased shielding of the sources on the upper surface of the star-board wing side and canard (farthest away from the microphones) is observed. Conversely, decreased shielding is noted for the leading edge and canard that are closer to the array.

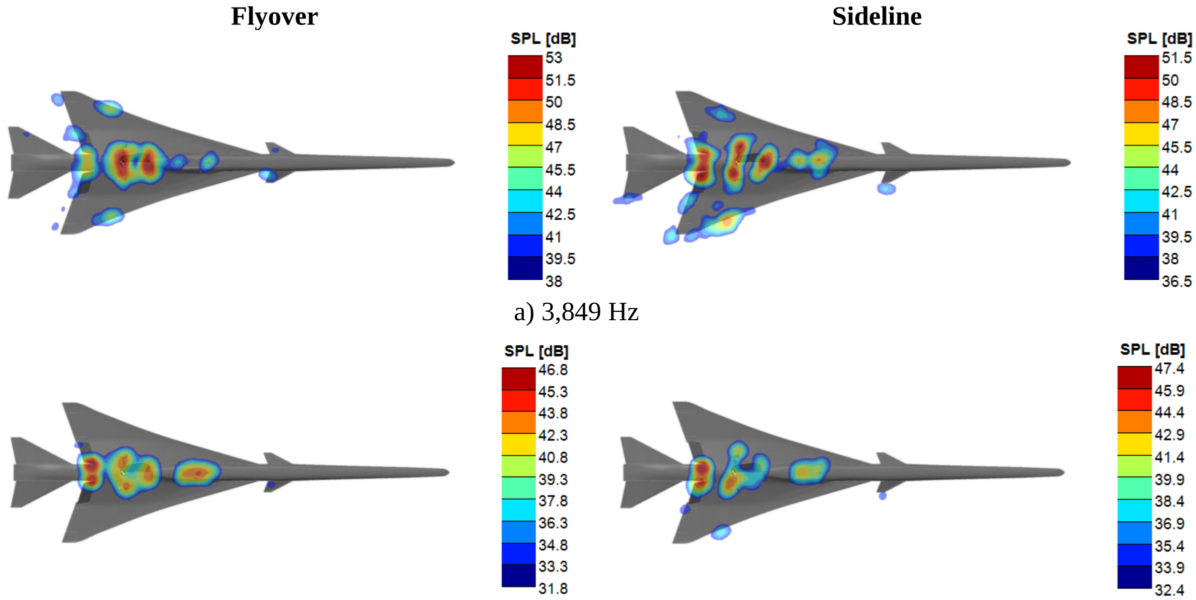

a) 3,849 Hz

b) 7,698 Hz

Fig. 38 Flyover and sideline CLEAN maps for Flap30-LGon configuration (medium resolution).

Integrated spectra for total noise and the three primary components are depicted in Fig. 39. Note from Fig. 39a that the total noise produced by the model ("Sum") remains unchanged to an observer positioned at the sideline angle used for the present analysis, partially confirming the lack of directivity for single microphone data observed in Ref. [12]. The main reason for this indifference is the modest change in noise produced by the MLG, NLG, and flaps, as evidenced in Figs. 39b through 39d. As noted in the beamform maps of Fig. 38, the largest differences occur for the leading edge and canard sources. Shown in Fig. 40 are the integrated spectra obtained from the leading and trailing edge regions on the port and starboard sides of the model, and the canards. On the port side (closer to the array, Figs. 40a and 40b), the noise levels are about 2 to 3 dB higher at the sideline than those overhead. Conversely, sideline levels from regions on the starboard side (Figs. 40c and 40d) are lower than overhead levels by approximately the same amount. As a result, addition of contributions from the port and starboard sides would yield nearly equivalent combined levels at each array (overhead and sideline). Whether coincidence or not, this behavior reinforces the lack of directionality in the GLBC far-field noise signature displayed in Fig. 39a and the directivity plots of Ref. [12]. The only components displaying some degree of dependency on emission angle are the canards. As shown in Fig. 40e, the noise levels produced by these components are lower in the sideline direction.

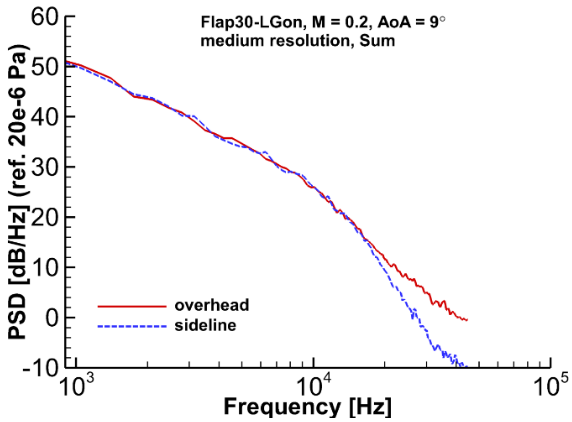

a) Sum

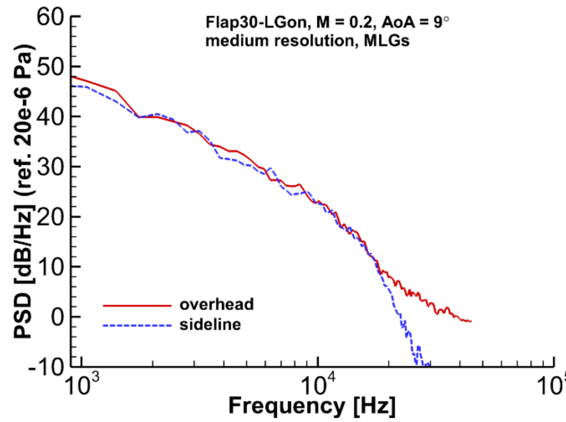

b) MLG

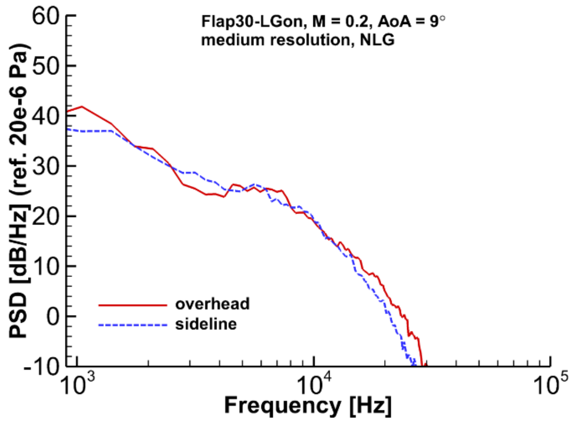

c) NLG

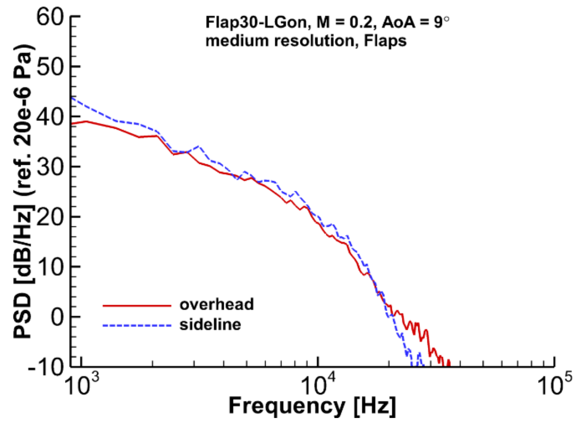

d) Flaps

Fig. 39 Flyover and sideline integrated spectra for Flap30-LGon configuration (medium resolution) – landing gear and flaps.

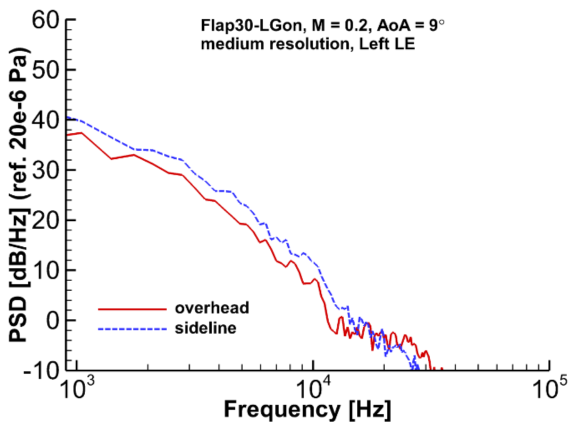

a) Left LE

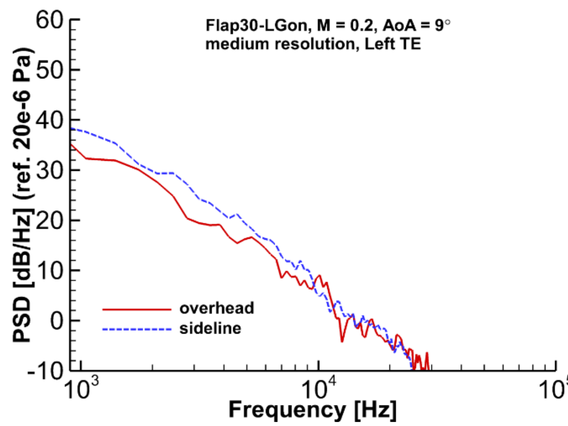

b) Left TE

Fig. 40 Flyover and sideline integrated spectra for Flap30-LGon configuration (medium resolution) – wing and canards.

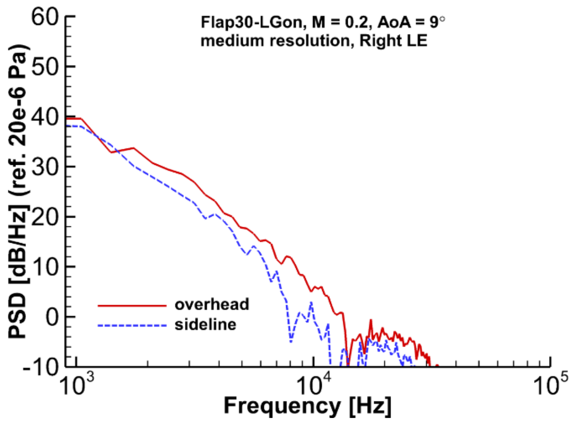

c) Right LE

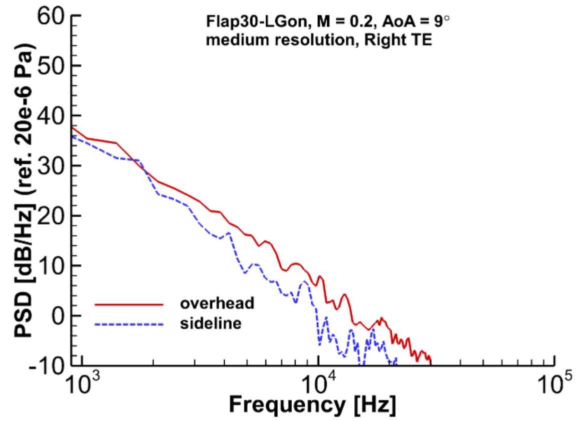

d) Right TE

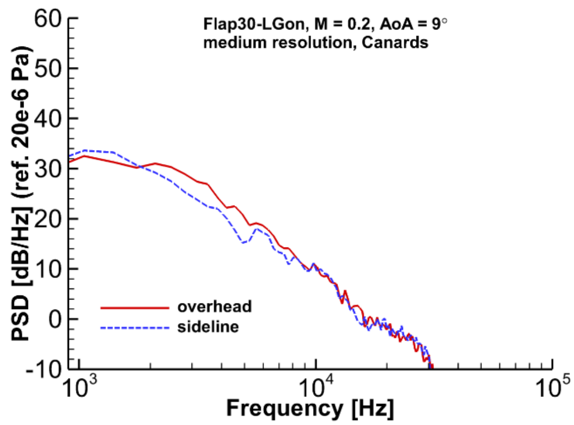

e) Canards

Fig. 40 Concluded.

6. Angle of Attack Effects

For conventional subsonic aircraft, airframe noise displays a weak dependency on AoA at the low to moderate angles typical of landing conditions [13]. To examine whether a similar trend holds for supersonic aircraft, a free-air, medium resolution simulation of the Flap30-LGon configuration for M = 0.2 and AoA = 6° was performed also. The resultant integrated spectra for the "Sum" and the three primary noise sources of the GLBC model are shown in Fig. 41. As can be observed from these plots, the total noise produced by the model, as well as the noise generated by the MLG, NLG, and flaps is independent of AoA (within the limited range examined here). However, the effects of AoA variation manifest differently when secondary noise sources are considered. Far-field spectra obtained from integration of the Canards, Right LE, and Right TE regions are presented in Fig. 42. The most significant change occurs for noise generated by the canards (Fig. 42a), with an 8 to 10 dB drop in levels at the lower AoA. While still substantial, a less dramatic reduction is observed for the noise produced at the leading and trailing edge regions of the wing (Figs. 42b and 42c). The noise from the tail remains unchanged (Fig. 42d).

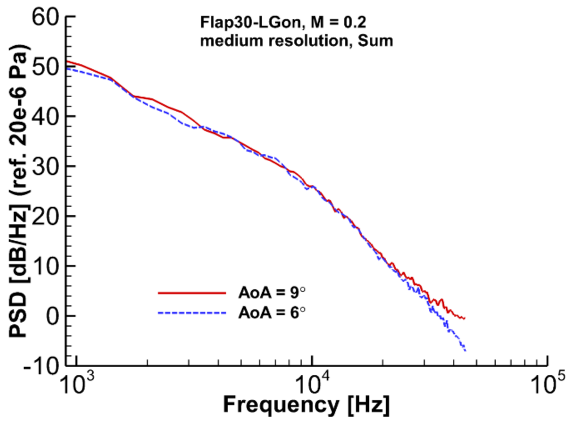

a) Sum

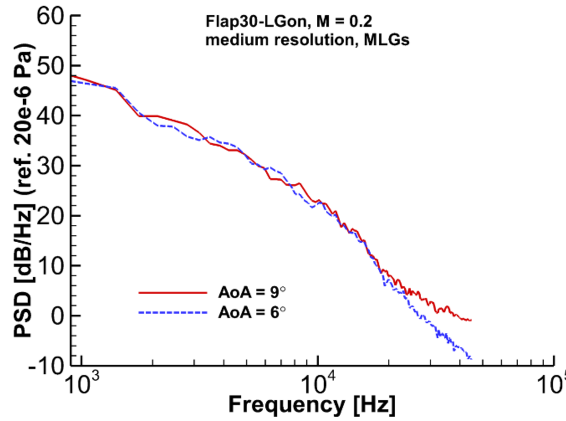

b) MLG

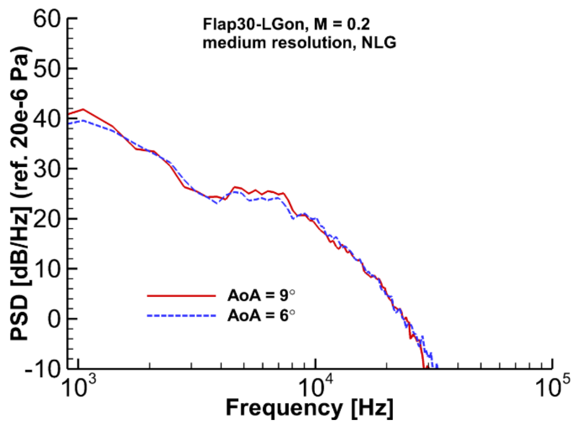

c) NLG

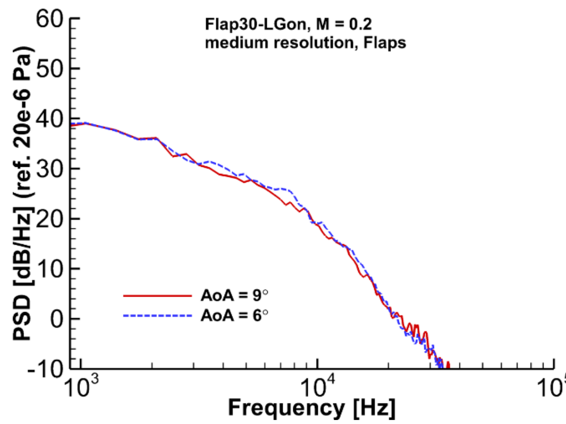

d) Flaps

Fig. 41 Effects of AoA on integrated spectra for Flap30-LGon configuration (medium resolution) – landing gear and flaps.

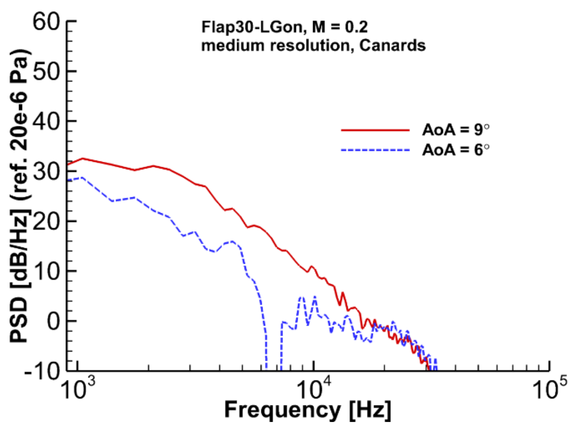

a) Canards

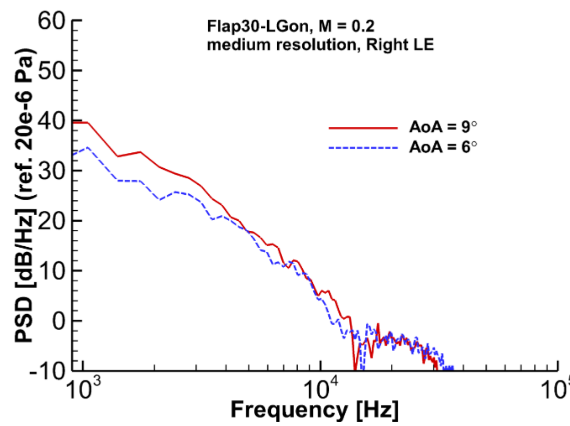

b) Right LE

Fig. 42 Flyover and sideline integrated spectra for Flap30-LGon configuration (medium resolution) – control surfaces and wing.

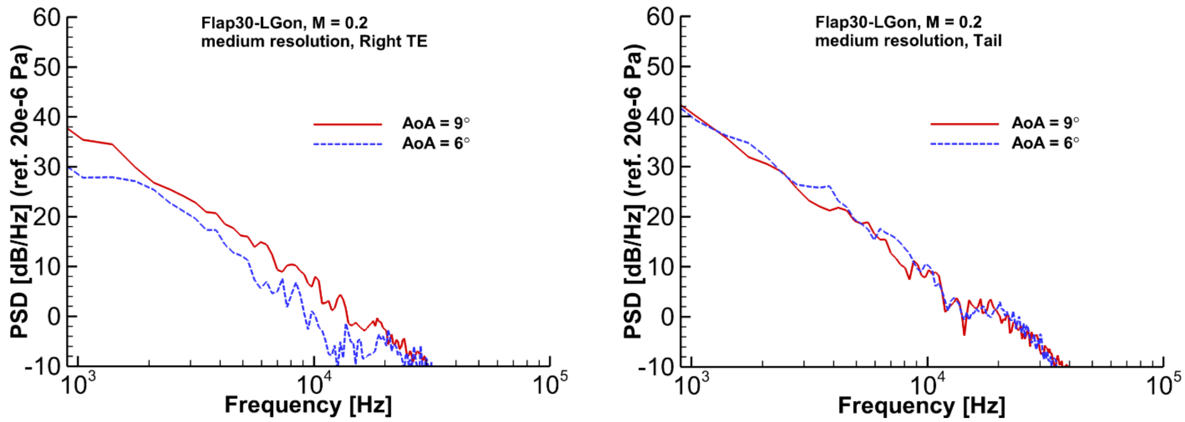

c) Right TE d) Tail

Fig. 42 Concluded.

7. Component Interaction Effects

As observed in Fig. 43, the GLBC is a compact design with several major airframe components – such as the nose and main landing gear, flap, and stabilator – in close proximity to each other and aligned in a manner that facilitates complex component interaction. The integrated far-field spectra from the "Sum" of all sources for the four GLBC configurations listed in Table 3 are presented in Fig. 44. The difference in levels between the noisiest (landing) and quietest (cruise) configurations is approximately 10 to 12 dB for frequencies up to 15 kHz, where accuracy of the predicted noise becomes less accurate due to insufficient spatial resolution in the simulations. Note that deflection of the flaps (Flap30-LGoff) adds about 5 dB to the spectrum of the cruise configuration. In contrast, the levels for the Flap0-LGon configuration fall within 1 dB of those for the Flap30-LGon, indicating that the noise produced by the undercarriage constitutes nearly 80% of the GLBC total airframe noise. To illustrate the impact of component interactions on far-field noise signatures, an additional GLBC configuration was simulated at medium spatial resolution. For this configuration, the model flaps were deflected 30°, the MLG deployed, but the nose landing gear was removed, and its cavity closed. The effects of flap retraction on MLG noise are displayed in Fig. 45a. Clearly, the MLG noise signature is not affected by flap deflection. In contrast, removal of the NLG significantly affects the MLG noise levels (Fig. 45b). That is, absence of the NLG reduces MLG noise by 1–2 dB at frequencies below 10 kHz, highlighting the complex interaction between the two components. Nose-main landing gear interaction is not an issue for conventional subsonic transports, even when smaller business jets are considered [8]. The impact of gear deployment on flap noise is demonstrated in Fig. 46. When both NLG and MLG are deployed (Fig. 46a), flap noise increased between 1–2 dB over a wide frequency range. However, with MLG deployed and NLG stowed (Fig. 46b), the flaps produced 2–3 dB more noise than the configuration with no gear present. Finally, the noise generated by the canards for the five configurations simulated are compared in Fig. 47. For four of the configurations, canard noise remained the same. However, for the Flap30-LGoff configuration, the noise increased by 4–5 dB over the 3 kHz – 15 kHz frequency range, suggesting a complex dependency of canard sources on deployment of other airframe components. Component interactions such as these are aircraft dependent. The changes in noise levels they cause are difficult to model and almost impossible to generalize. As a result, nearly all semiempirical airframe noise prediction models may fail to properly capture the noise signatures produced by individual components.

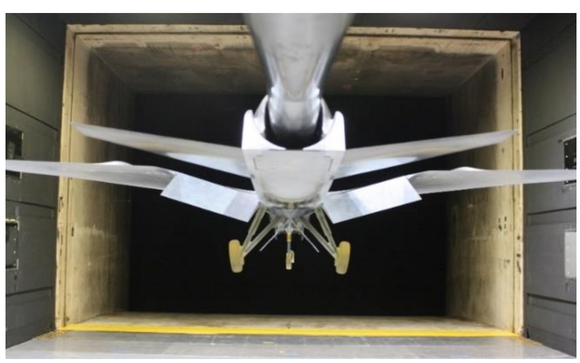

Fig. 43 Rear view of the GLBC model in landing (Flap30-LGon) configuration.

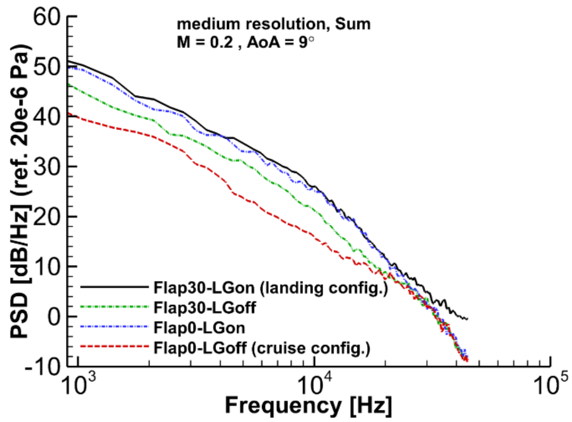

Fig. 44 Integrated total noise spectra for various GLBC configurations (medium resolution).

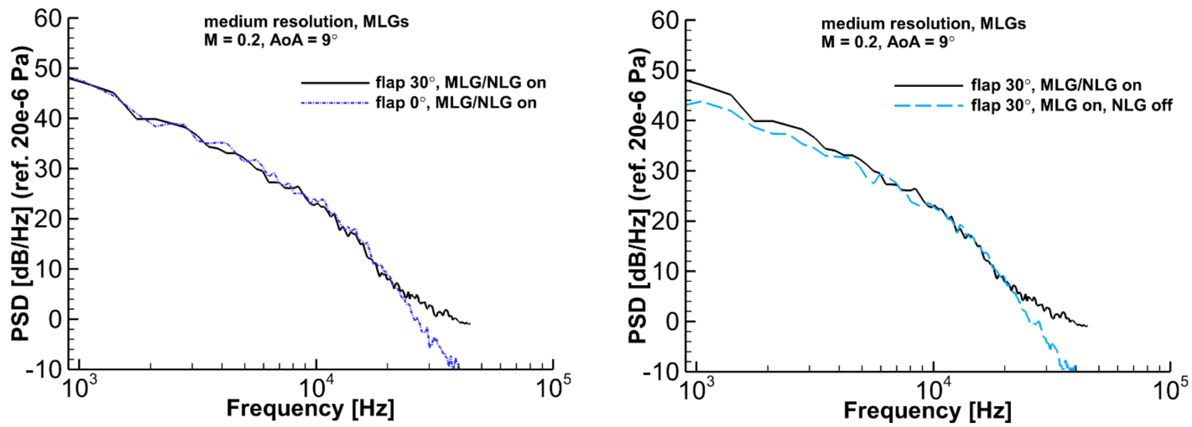

a) Flap effects b) NLG effects

Fig. 45 Effects of flap and NLG components on MLG noise levels (medium resolution).

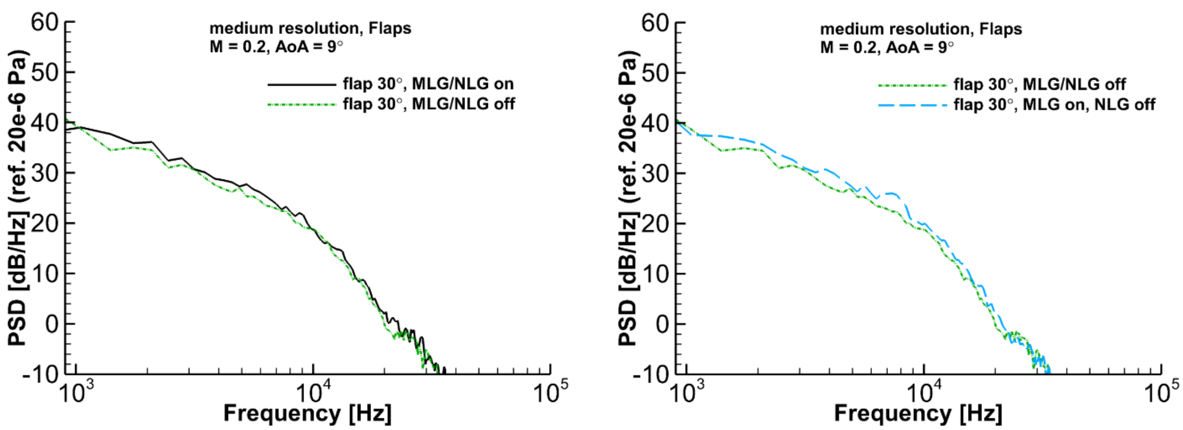

a) MLG and NLG effects b) MLG effects

Fig. 46 Effects of MLG and NLG components on flap noise levels (medium resolution).

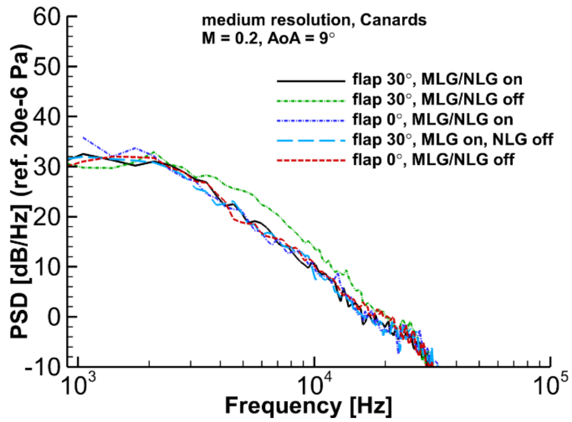

Fig. 47 Effects of various airframe components on canard noise levels (medium resolution).

8. Velocity Scaling for Far-field Noise Levels

To determine an appropriate velocity scaling for far-field noise, medium resolution simulations at additional speeds were performed for the Flap30-LGon and Flap0-LGoff configurations. Unscaled integrated spectra for the "Sum" of all GLBC sources are shown in Fig. 48 for both model configurations. For the quietest condition (cruise, Fig. 48b), results for the two lowest speeds show flattening of the spectral roll-off at frequencies close to 10 kHz, suggesting possible contamination from numerical sources that cause SNR degradation. We will examine this issue in the next section.

For conventional subsonic transports, airframe noise levels typically follow an M^6 velocity scaling without the need to apply frequency (or Strouhal, St) scaling. In Ref. [12], based on single-microphone data, M^6 without St scaling produced the best collapse for far-field total noise spectra obtained at various speeds. The availability of synthetic array data has allowed us to reexamine velocity scaling and extend it to the noise produced by individual airframe components. For the present study, we analyzed various exponents – 5, 5.5, 6, and 6.5 – and found also that M^6 provides the best collapse for the predicted levels. With M = 0.2 as the nominal value, the normalized spectra without and with St scaling for the "Sum" and several GLBC components are shown in Fig. 49 for the Flap30-LGon configuration. Without frequency scaling (Fig. 49a), total "Sum" spectra display good collapse of the noise levels at frequencies below 4 kHz. Above 4 kHz, spectral collapse degrades. The application of St scaling produces an opposite trend. That is, good spectral collapse is achieved for the frequency range of 4 kHz – 12 kHz and suboptimal collapse below 4 kHz (Fig. 49b). We note that St scaling applies to both frequency and amplitude since PSD is expressed in dB/Hz. Very similar trends are observed for the noise produced by the MLG and NLG (Figs. 49c through 49f). Such behavior is expected, since GLBC total noise is dominated by landing gear sources. Because the undercarriage used for the model is very rudimentary (composed of several simple bluff bodies), we suspect that a sizable portion of the noise generated by the gear stems from regular vortex shedding, which tends to follow a St normalization. Flap noise behaves differently, and M^6 combined with St scaling produce a good spectral collapse up to 15 kHz, where adequate spatial resolution is maintained (Figs. 49g and 49h). Different trends are observed when the noise generated at the wing leading edges and canards is examined (Figs. 50a through 50d). For these sources, a reasonably good spectral collapse was attained with M^6 alone. Application of St scaling significantly degraded the results.

Scaling of the noise generated by the Flap0-LGoff configuration also showed mixed trends. Scaled far-field spectra for the cruise configuration are shown in Fig. 51. As can be seen in Figs. 51a and 51b, M^6 without St scaling produces better data collapse that extends to higher frequencies. A similar observation holds for the noise generated by the canards (Figs. 51c and 51d), where M^6 scaling alone provides a better outcome. The trend reverses when wing leading edge noise is examined. Here, the combination of M^6 with St scaling produces much better results. Note that the latter trend is opposite to that observed for the leading-edge sources of the Flap30-LGon configuration (see Figs. 50c and 50d). The causes of this reversal are not clear to us, since the noise generation mechanism and emerging sources are the same for both configurations. A possible, physical explanation may be that, since undercarriage noise is so prominent for Flap30-LGon, its reflection off the wing undersurface may also be substantial and contributed to leading-edge noise when integration of the beamform maps for Left, Right, LE and TE regions was performed. The causes of this trend may also be numerical. As mentioned earlier, the large difference in amplitude between primary and secondary noise sources may cause contamination of the integrated levels for the latter by contributions from spurious sources.

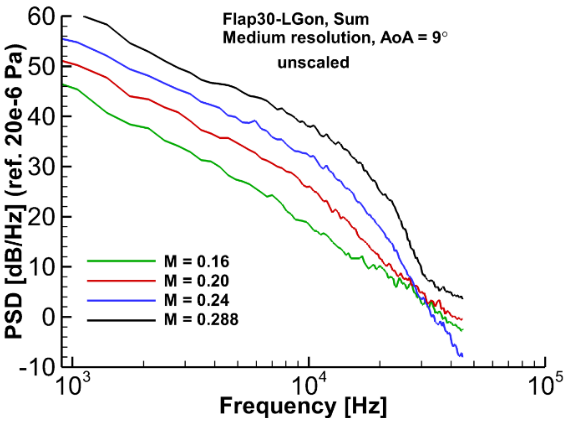

a) Flap30-LGon (landing)

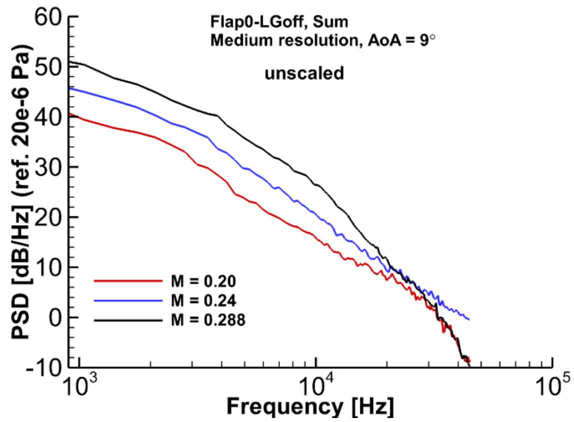

b) Flap0-LGoff (cruise)

Fig. 48 Unscaled integrated total noise spectra at different speeds for landing and cruise configurations (medium resolution).

M^6 scaling

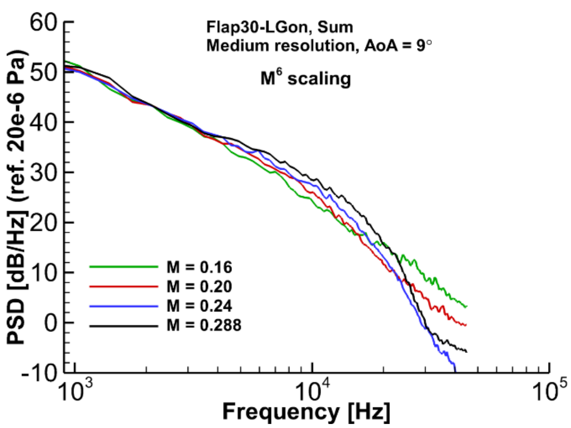

a) Sum

M^6 and St scaling

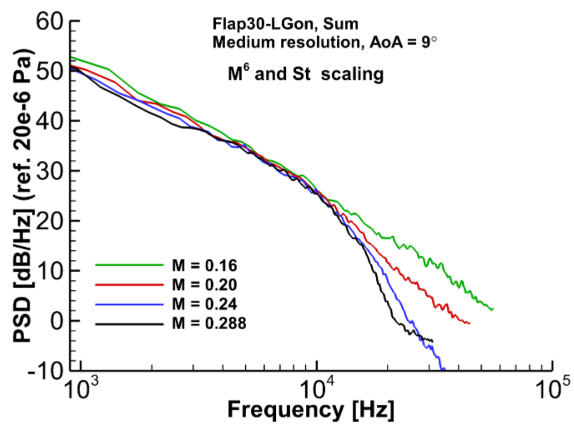

b) Sum

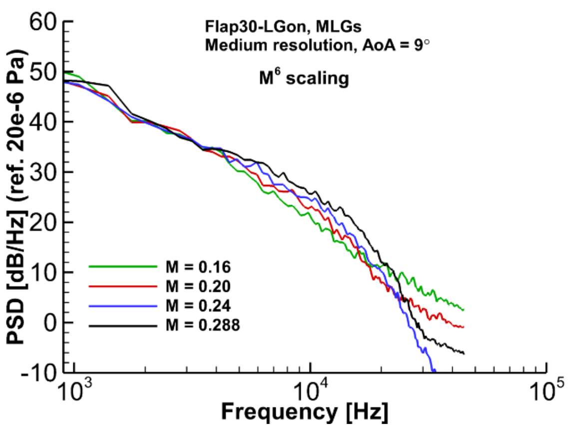

c) MLG

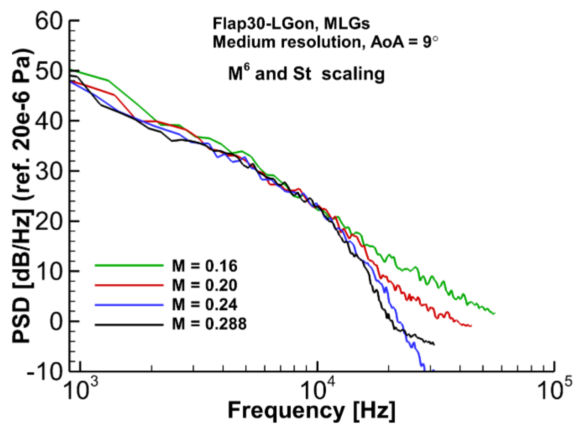

d) MLG

Fig. 49 Scaled integrated spectra for Flap30-LGon configuration (medium resolution) – landing gear and flaps.

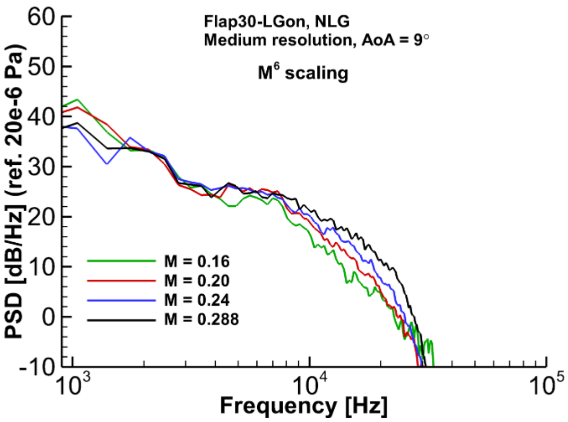

e) NLG

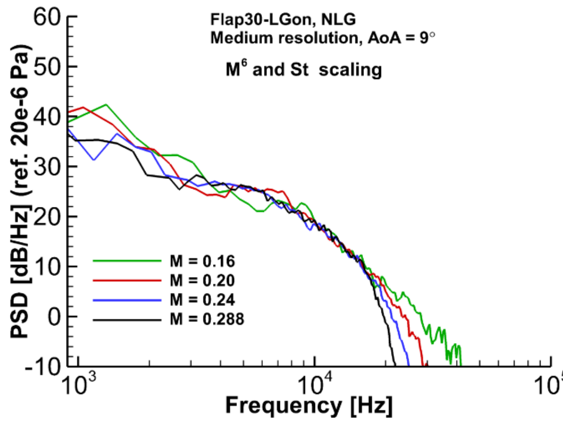

f) NLG

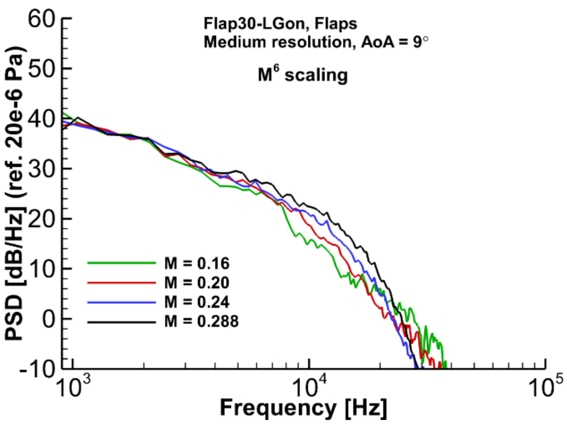

g) Flaps

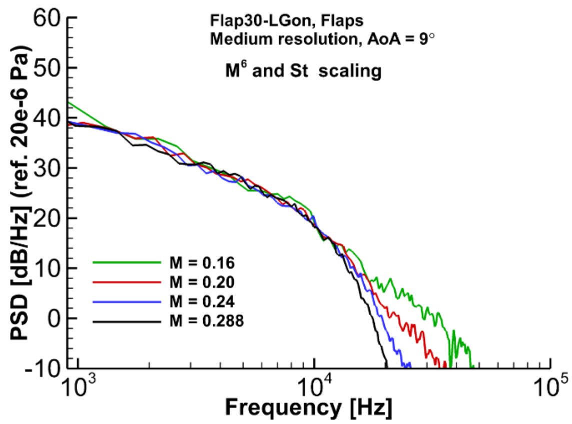

h) Flaps

Fig. 49 Concluded.

M^6 scaling

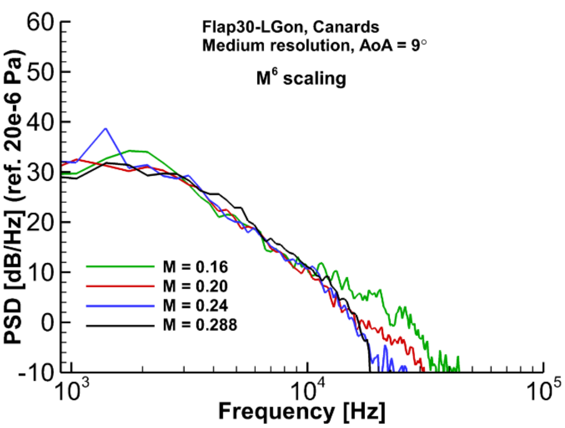

a) Canards

M^6 and St scaling

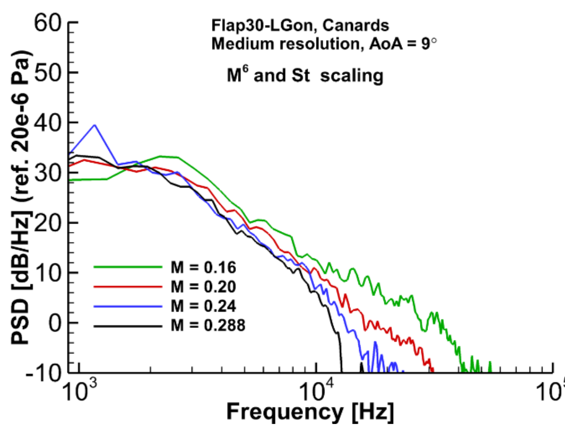

b) Canards

Fig. 50 Scaled integrated spectra for Flap30-LGon configuration (medium resolution) – canards and wing.

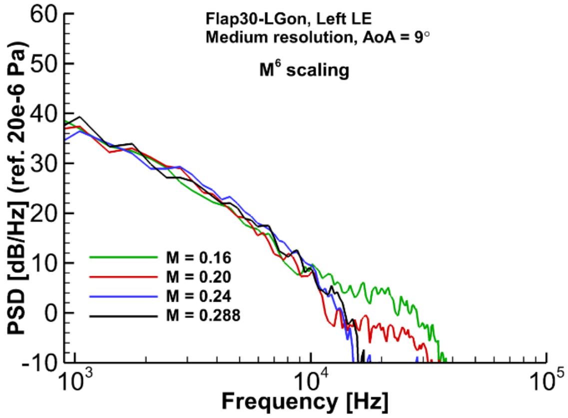

c) Left LE

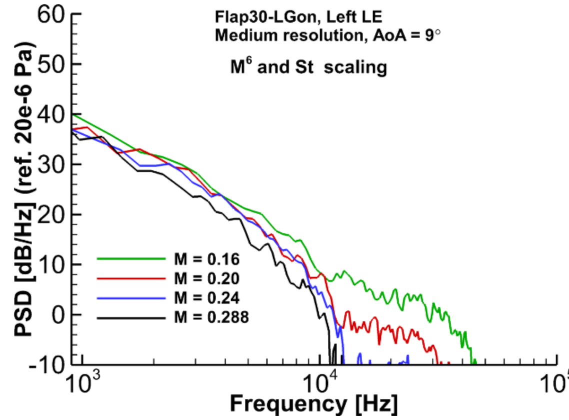

d) Left LE

Fig. 50 Concluded.

M^6 scaling | **M^6 and St scaling**

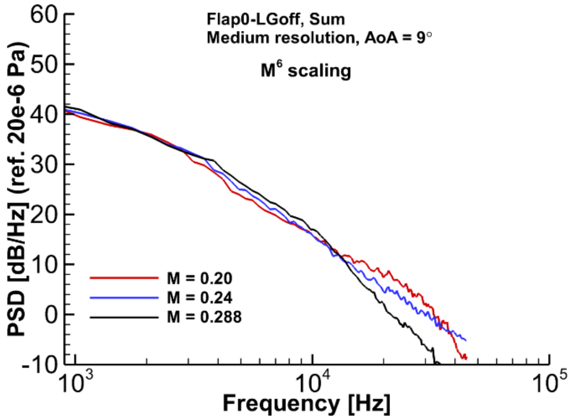

a) Sum

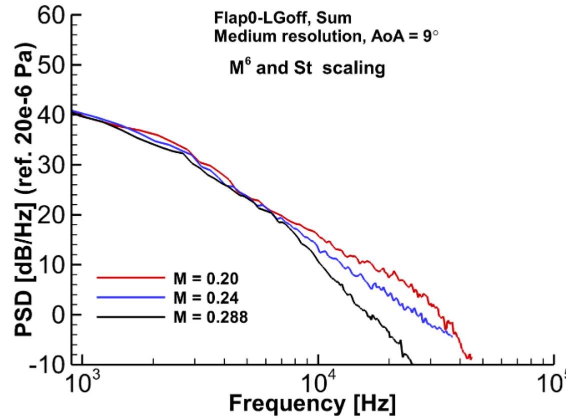

b) Sum

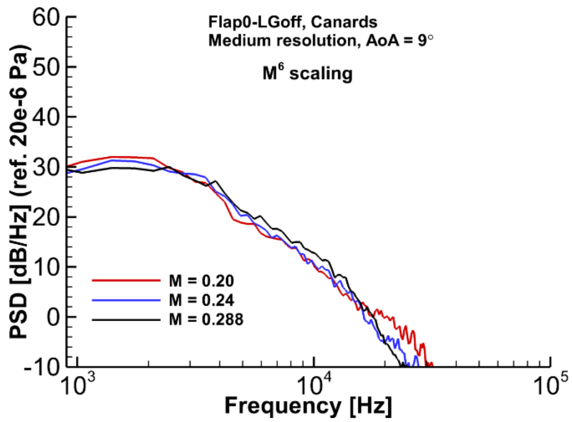

c) Canards

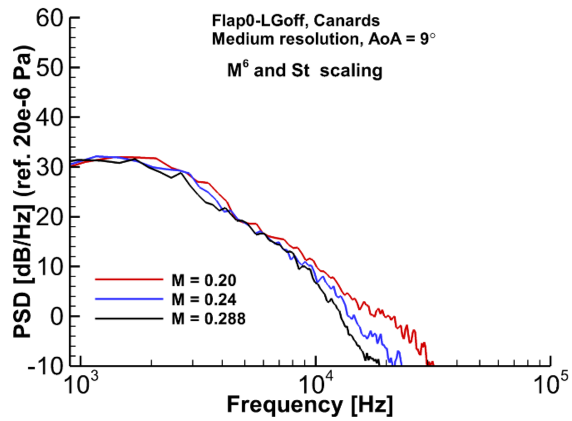

d) Canards

Fig. 51 Scaled integrated spectra for Flap0-LGoff configuration (medium resolution) – canards and wing.

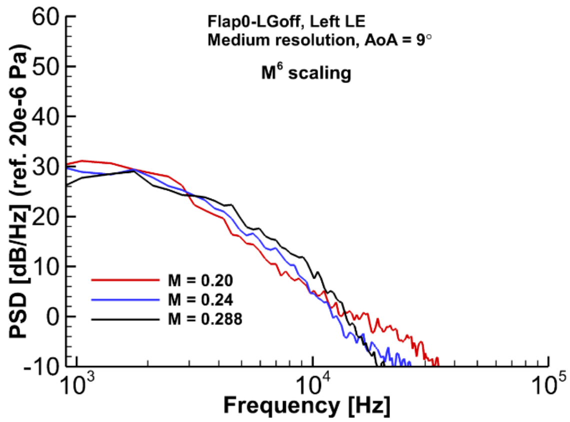

e) Left LE

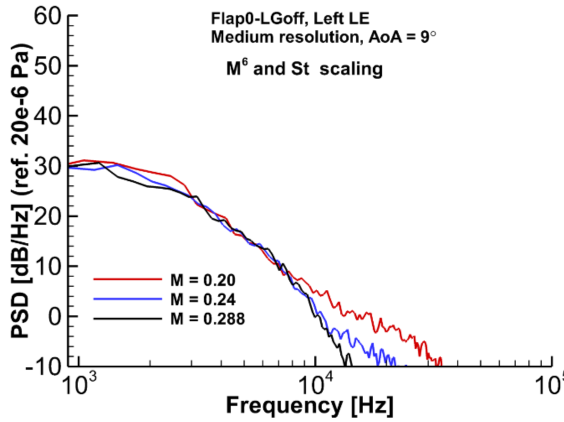

f) Left LE

Fig. 51 Concluded.

9. Impact of Numerical Precision on Noise

All simulations used in the aerodynamic and acoustic analyses presented here were performed in single precision. As observed in Fig. 48b, the spectral roll-off at higher frequencies for the Flap0-LGoff configuration suggested the presence of numerical noise, which may degrade the SNR for the computed physical sources. To further examine this issue, the coarse resolution simulation of this configuration was repeated using double precision. As reported in Ref. [12], the resulting far-field spectrum showed a marked improvement at higher frequencies, where the noise levels are low. To highlight the effect of numerical sources and low SNR, CLEAN maps obtained from single and double precision coarse simulations of the Flap0-LGoff configuration are shown in Fig. 52. For frequencies below 8 kHz, both simulations produced very similar source maps (Fig. 52a). At frequencies close to 10 kHz (Fig. 52b), the single precision maps show the appearance of numerical (unphysical) sources that may contribute substantially to the integrated spectra. At frequencies close to 15 kHz (Fig. 52c), the single precision results contain numerical sources that overwhelm the beamform maps, resulting in significant overprediction of the spectral levels when integration of the maps is performed. In stark contrast, the maps obtained from the double precision simulation effectively suppress numerical noise, allowing a much cleaner picture of the physical sources to emerge. Corresponding integrated far-field spectra for the total "Sum" noise and the noise generated by the Canards and Left LE regions are presented in Fig. 53. For completeness, spectra from single precision, medium resolution simulations were also included in these plots. Notice that, for the model total noise (Fig. 53a), the effect of numerical precision becomes apparent at slightly lower frequencies than those observed for the GLBC canards (Fig. 53b). Also note that increasing spatial resolution is not as effective as higher numerical precision in elevating the SNR when the noise levels produced by physical sources are low. To illustrate the impact of source strength on SNR, CLEAN maps from single-precision, medium resolution simulations for the three speeds examined are compared in Fig. 54. Observe that, as the physical sources gain strength with increasing speed, contamination from numerical noise falls below the 15 dB cutoff threshold and allows cleaner source maps to emerge. Finally, we note that executing a PowerFLOW® simulation in double precision approximately doubles the computational cost and time needed to obtain a converged solution. Given the number of configurations (see Table 3) and computational grid sizes used in the present study [12], the advantages and disadvantages of such a decision must be weighed carefully.

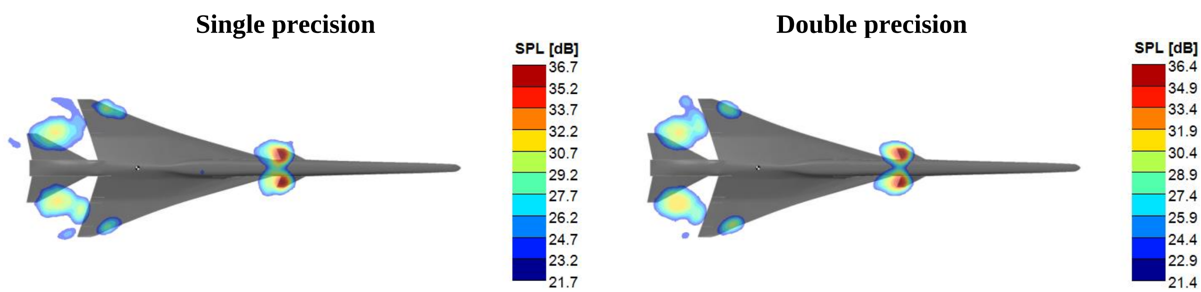

a) 7,687 Hz

Fig. 52 Effect of numerical precision on CLEAN maps for Flap0-Lgoff configuration (coarse resolution).

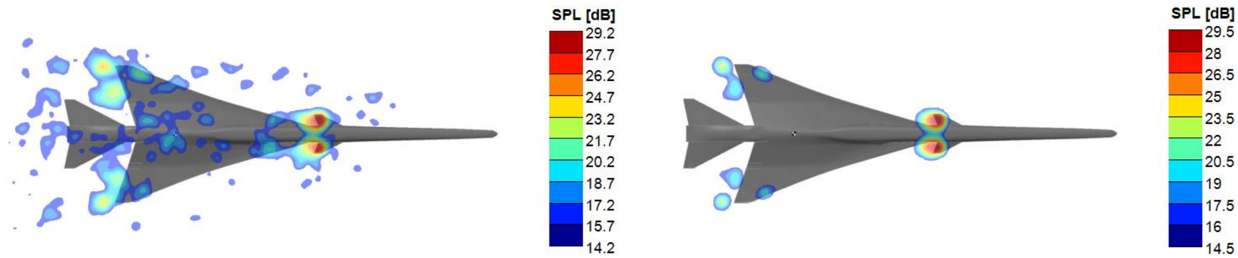

b) 10,831 Hz

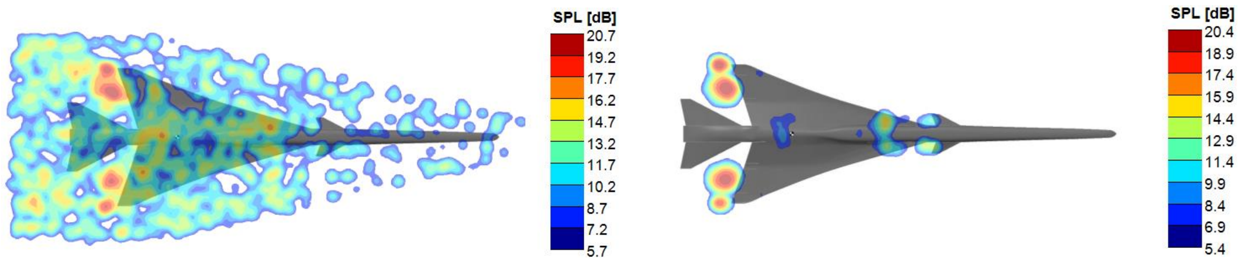

c) 15,024 Hz

Fig. 52 Concluded.

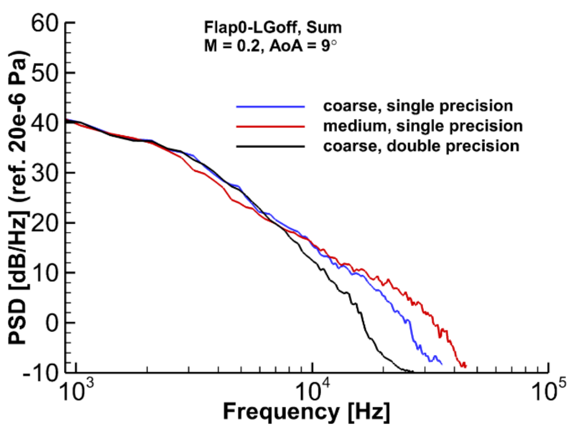

a) Sum

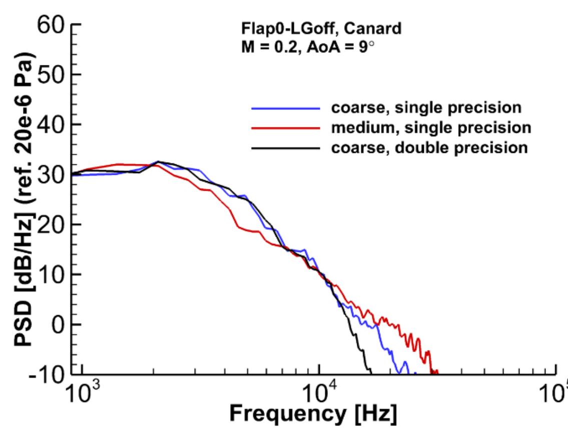

b) Canards

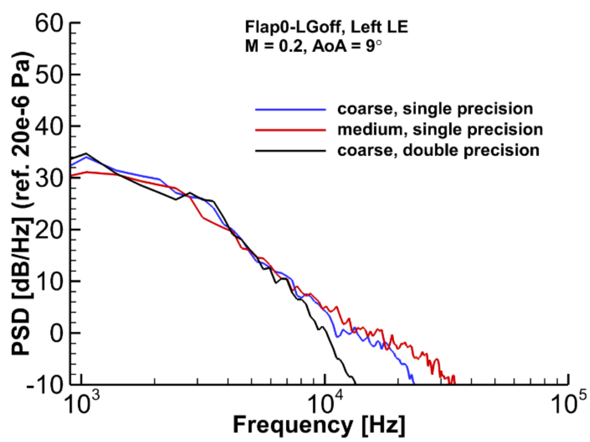

c) Left LE

Fig. 53 Effect of numerical precision on integrated spectra for Flap0-LGoff configuration.

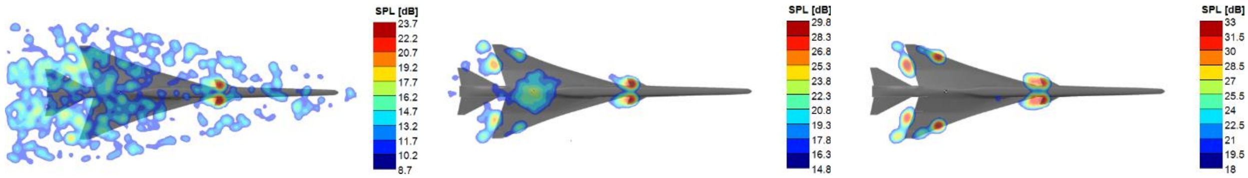

a) M = 0.2 b) M = 0.24 c) M = 0.288

Fig. 54 Effects of speed on SNR for sound sources of Flap0-LGoff configuration (15 kHz, medium resolution).

VI. Summary

In-depth knowledge of the noise generated by commercial supersonic aircraft during takeoff and landing operations is necessary to develop the standards and metrics that will regulate the impact of this type of aircraft on communities near airports. Currently, the sources of airframe noise for supersonic vehicles are poorly understood. The present investigation is a first step in a focused effort by NASA to create a much-needed database on the airframe component of noise generated by commercial supersonic transports and, thus, improve the state-of-the-art in noise prediction. As a preliminary effort to remedy this knowledge gap, a detailed aeroacoustic study of a generic low-boom concept (GLBC) was performed.

An extensive aerodynamic test of a 15%-scale model of the GLBC was conducted in the NASA LaRC 14- by 22-Foot Subsonic Tunnel to determine the stability and control characteristics of the design. Although no acoustic data were obtained, sufficient information was available to validate predicted aerodynamic trends prior to commencing costly airframe noise simulations. Measured lift, drag, and pitching moment coefficients, and limited steady surface pressures were used to demonstrate that good data quality and repeatability were attained during the test.

For a direct comparison with measurements, the entire tunnel test section plus the model support system were included in the aerodynamic simulations of the GLBC. To determine the accuracy of the predicted results, simulations for all configurations were conducted at two grid resolutions. A third grid resolution was also used to simulate the landing configuration (flap 30° and landing gear deployed) at AoA = 9°. Overall, good agreement between simulated and measured force coefficients was attained. In most instances, the agreement improved with increased spatial resolution. Good correspondence between simulated and measured steady surface pressures was also achieved. Although the agreement in pressure distribution improved with grid resolution, convergence of the predicted pressures toward the measured distribution was slow and highlights some of the intrinsic challenges associated with the accurate resolution and capture of vortex-dominated flows such as those encountered on low aspect ratio, supersonic wings. Favorable comparisons between in-tunnel simulated results and those obtained in free-air revealed that blockage effects on measured aerodynamic data were negligible.

An AoA of 9° was selected for all airframe noise simulations. A synthetic array comprising eight hundred microphones was implemented in overhead and sideline positions to conduct detailed acoustic analyses of the GLBC model. Data on both permeable and solid surfaces were used as input to an FW-H formulation to generate the requisite pressure records at the microphone locations. The usage of end caps in the permeable surface failed to minimize the hydrodynamic effect of flow structures passing through the outlet plane of the permeable data surface. Convection of large-scale longitudinal vortices, formed at the wing leading edges, through the end caps resulted in the production of strong numerical sources that contaminated the high-frequency content of the far-field noise spectra. Through careful evaluation, we demonstrated that use of an open-ended penetrable data surface is an effective way to remove end cap effects without affecting the physical noise signature of the GLBC. CLEAN beamform maps were used to demonstrate the inadequacy of solid surface data when shielding effects are important – significant overprediction of integrated far-field noise spectra was observed.

Far-field noise spectra extracted from integration of the CLEAN maps on carefully tailored regions of the aircraft indicated that the MLG is the dominant source of noise for this aircraft. Together with the NLG, they account for nearly 80% of the total GLBC noise. Flap noise levels were comparable to those for the NLG. The secondary airframe noise sources were the canards, wing leading edges, and tail. These latter sources are unique to supersonic configurations and have no equivalent in conventional, subsonic transports.

The noise produced by the primary sources was unaffected by modest variations in AoA and followed established trends for subsonic transports. However, due to the compact design of supersonic aircraft, component interactions significantly affect the noise levels produced by the individual airframe components. Lastly, an M^6 scaling yielded the best collapse of far-field noise levels obtained at different aircraft speeds. However, unlike subsonic transports, this scaling failed to collapse the spectral levels across the entire frequency range. Application of Strouhal scaling to the frequencies improved data collapse for certain portions of the frequency range of interest. This mixed effect was attributed to the rudimentary geometry of the landing gear that promotes strong bluff body vortex shedding.

Acknowledgments

This work was supported by the Commercial Supersonic Technology project under the Advanced Air Vehicles Program of the NASA Aeronautics Research Mission Directorate. The authors would like to thank the staff of the Langley 14 x 22 tunnel facility for their outstanding support and execution of a highly productive test entry. We also gratefully acknowledge the invaluable contribution of Scott Brynildsen of Craig Technologies for his patience with the tedious task of creating the CAD definitions for the model landing gear and support system, as well as for cleaning and integrating the various aircraft components into a CFD-ready representation. All simulations were performed on the computer clusters at the NASA Advanced Supercomputing (NAS) facility at the Ames Research Center. The logistical support provided by NAS staff, in particular Yan-tyng (Sherry) Chang, is greatly appreciated.

References

[1] Spike Aerospace, Inc, [URL: https://www.spikeaerospace.com/, retrieved June 2021].

[2] Boom Technology, Inc., [URL: https://boomsupersonic.com/, retrieved October 2020].

[3] Berton, J. J., Huff, D. L., Seidel, J. A., and Geiselhart, K. A., "Supersonic Technology Concept Aeroplanes for Environmental Studies," AIAA Paper 2020-0263, January 2020.

[4] Preisser, J. S., "Airframe Noise Measurements on a Supersonic Transport Small-Scale Model," *J. Aircraft*, Vol. 17, No. 11, pp. 795-801, November 1980.

[5] Herkes, W. H. and Stoker, "Wind Tunnel Measurements of the Airframe Noise of a High-speed Civil Transport," AIAA Paper 98-0472, January 1998.

[6] Khorrami, M.R. and Fares, E. "Toward noise certification during design: airframe noise simulations for full-scale, complete aircraft", *CEAS Aeronaut J.* (2019) 10: 31. doi:10.1007/s13272-019-00378.

[7] Ferris, R. J., Appelbaum, J., and Khorrami, M. R., "Simulations of a Full-Scale Aircraft with Installed Airframe Noise Reduction technologies," AIAA Paper 2018-2974, June 2018.

[8] Duda, B., Ferris, R. J., and Khorrami, M. R., "Simulation-Based Assessment of a Full-Scale Installed Quiet Landing Gear," AIAA Paper 2019-2476.

[9] Khorrami, M. R., Ravetta, P. A., Lockard, D. P., Duda, B., and Ferris, R., "Comparison of Measured and Simulated Acoustic Signatures for a Full-Scale Aircraft with and without Airframe Noise Abatement," AIAA Paper 2018-2975, June 2018.

[10] NASA Aeronautics Research Mission Directorate, [URL: https://www.nasa.gov/X59, retrieved October 2020].

[11] Ferris, R., Sacks, M., Cerizza, D., Ribeiro, A. F. P., and Khorrami, M. R., "Aeroacoustic Computations of a Generic Low Boom Concept in Landing Configuration: Part 1 - Aerodynamic Simulations," Paper to be presented at AIAA/CEAS Aeroacoustics Conference, August 2021.

[12] Ribeiro, A. F. P., Ferris, R., and Khorrami, M. R., "Aeroacoustic Computations of a Generic Low Boom Concept in Landing Configuration: Part 2 - Airframe Noise Simulations," Paper to be presented at AIAA/CEAS Aeroacoustics Conference, August 2021.

[13] Khorrami, M. R., Humphreys, Jr. W. M.., and Lockard, D. P., "An Assessment of Flap and Main Landing Gear Noise Abatement Concepts," AIAA Paper 2015-2987, June 2015.

[14] Ravetta, P. A., Khorrami, M. R., König, B., and Fares, E., "Multiplanar Synthetic Arrays and Their Application to Full-Scale Landing Gear Noise Source Identification," paper to be presented at the 27th AIAA/CEAS Aeroacoustics Conference, August 2021.

[15] Khorrami, M. R., Humphreys, Jr. W. M.., Lockard, D. P., and Ravetta, P. A., "Aeroacoustic Evaluation of Flap and Landing Gear Noise Reduction Concepts," AIAA Paper 2014-2478, June 2014.

[16] Ffowcs Williams, J. E., and Hawkings, D. L., "Sound Generation by Turbulence and Surfaces in Arbitrary Motion," Philosophical Transactions of the Royal Society of London, Series A, Mathematical and Physical Sciences, Vol. 264, No. 1151, 1969, pp. 321–342.

[17] Sijtsma, P., "CLEAN based on Spatial Source Coherence," AIAA Paper 2007-3436, May 2007.

[18] AVEC Phased Array Software, Ver 5.8, AVEC, Inc., Blacksburg, VA, URL: https://www.avec-engineering.com/products.html [cited June 2021].

[19] König, B., Fares, E. Ravetta, P. A., and Khorrami, M. R., "A Comparative Study of Simulated and Measured Main Landing Gear Noise for Large Civil Transports," AIAA Paper 2017-3013, June 2017.

[20] Spalart, P.R., Belyaev, K.V., Shur, M.L., Strelets M.K., Travin, A.K., "On the differences in noise predictions based on solid and permeable surface Ffowcs Williams–Hawkings integral solutions," *International Journal of Aeroacoustics*. 2019;18(6-7):621-646. doi:10.1177/1475472X19878934

[21] Fares, E., König, B., and Khorrami, M. R., "Effect of Geometric Granularity on the Noise Signature of a Full-Scale Large Civil Transport Nose Landing Gear," paper to be presented at the 27th AIAA/CEAS Aeroacoustics Conference, August 2021.